University
of Dundee

University of Dundee

Biosynthesis of the ZnO/SnO2 nanoparticles and characterization of their photocatalytic potential for removal of organic water pollutants

Sayadi, Mohammad Hossein; Ghollasimood, Sholeh; Ahmadpour, Najmeh; Homaeigohar, Shahin

Link to publication in Discovery Research Portal

1   **Biosynthesis of the ZnO/SnO$_2$ nanoparticles and characterization of their photocatalytic**

2   **potential for removal of organic water pollutants**

3

4   **Mohammad Hossein Sayadi*[a,b], Sholeh Ghollasimood[c], Najemeh Ahmadpour[a], Shahin**

5   **Homaeigohar [d]**

6   [a] Department of Environmental Engineering, Faculty of Natural Resources and Environment,
7   University of Birjand, Birjand, Iran
8   [b] Department of Environmental Engineering, Faculty of Agriculture and Natural Resources,
9   Ardakan University, Ardakan, Iran
10   [*c] Pasture and Watershed Dep., Faculty of Natural Resource and Environment, University of Birjand, Birjand, Iran
11   [d] School of Science and Engineering, University of Dundee, DD1 4HN, UK
12   Corresponding author: mh_sayadi@birjand.ac.ir

13

14

15   **Abstract**

16   Plants are rich sources of antioxidant compounds including phenols and flavonoids. These

17   antioxidants are crucial elements in diet and protect the body against oxidative stress. In this

18   study, antioxidant activity of the phenolic compounds and flavonoids of mistletoe (*Viscum*

19   *album*), as a substituent for synthetic antioxidants, was quantitively investigated. The plant

20   alcoholic (ethanol) extract was used for biosynthesis of the ZnO/SnO$_2$ composite nanoparticles

21   that were employed for photodegradation of three organic pollutants (Congo red (CR), Biphenyl

22   A (BPA), and tetracycline (TC)) under solar light. The photodegradation tests were performed

23   considering the effect of pH, photocatalyst dosage, temperature, and initial concentration of the

24   pollutants. The obtained data were analyzed by a Pseudo-first-order kinetic model. The most

25   optimum conditions for photodegradation of the organic pollutants were found to be: 5 mg/l

26   initial pollutant concentration, 0.5 g/l photocatalyst dosage, and acidic pH. The reusability test

27   implied that the nanoparticles remain stable and can perform well even after 4 cycles of reuse.

28   Conclusively, *Viscum album* extract offers promising antioxidant properties and allows for

29   biosynthesis of the composite nanoparticles that can optimally photodegrade organic pollutants

30   of wastewater under solar light.

31

32   **Keywords:** antioxidants, *Viscum album*, photocatalytic degradation, biosynthesis, composite

33   nanoparticles.

34

1. Introduction

Rapid urbanization and industrialization across the world have led to vast environmental pollution, threatening the health of human kind. Human activities result in the release of over 300 million tons of organic and toxic pollutants into water streams each year, thereby endangering the health of human being and other creatures [1]. Due to the growing concern about the presence of organic pollutants in water, quality control against hazardous pollutants has become more stringent in many countries [2]. In addition, many new uncontrollable organic pollutants are continuously discharged into the environment [3], and can be found even in the drinking water. Therefore, development of novel, environmentally friendly methods to eliminate such organic pollutants is of utmost importance. In this regard, advanced and cost-effective technologies are required to remove these contaminants from wastewater [4]. Advanced Oxidation Processes (AOPs) are of the recommended technologies for the removal of a wide range of resistant and non-biodegradable organic pollutants. These processes can be also used as a pre-treatment method to increase the biodegradability of wastewater pollutants. Organic pollutants are mainly degraded by the hydroxyl radicals generated during the AOPs, that are highly reactive and selectively degrade almost all organic matters in water [5, 6]. As a well-known AOP, photodegradation involves the use of photocatalysts such as ZnO nanoparticles. This type of photocatalyst has been widely used for photodegradation of organic pollutants, mainly due to its non-toxicity, optimum electronic and catalytic properties, chemical stability, and the ability to transform solar energy to chemical energy for water treatment [7]. The use of ZnO nanoparticles has been widely reported due to its wide energy gap and higher efficiency in electron production, leading to photogeneration of holes for the efficient treatment of organic pollutants [8, 9]. However, due to rapid recombination of charge carriers, the photocatalytic activity of ZnO is limited. To address this problem, ZnO is typically coupled with other semiconductor materials, thereby lowering the electron-hole recombinant rate and increasing its photocatalytic efficiency [10]. The simultaneous use of two semiconductors such as TiO_2 – ZnO [11], ZnO-CuS [12], ZnO -WO_3 [13], and ZnO-CdS [14] has been already studied. Among the studied metal oxides, tin dioxide (SnO_2) has been shown to be a better electron receptor than ZnO due to its more positive conduction edge [15]. When coupled, it might reduce the electron-hole recombination rate of ZnO and thus improve its photocatalytic activity [16, 17].

65   ZnO based photocatalytic nanocomposites have been traditionally produced through

66   synthetic approaches involving the potentially hazardous chemicals. For instance, ZnO–Mg [18],

67   Co_3O_4–ZnO [19], CuO/ZnO [20], CeO_2–ZnO [21], ZnO–SnO_2 [22], WO_3/SnO_2, TiO_2/SnO_2 [23],

68   V_2O_5/ZnO, and ZnO/γ-Mn_2O_3 nanocomposites [24, 25] have been synthesized through thermal

69   decomposition, sol-gel, and hydrothermal method. To avoid the adverse consequences of the use

70   of chemicals, in the recent years, nanocomposite photocatalysts have been innovatively created

71   by employing the environmentally friendly, green materials [26]. Particularly, ZnO nanoparticles

72   have been recently biosynthesized by implementation of fungi, bacteria, plants, algae, among

73   others. Among the mentioned bioreactors, plant extracts are highly favorable due to their

74   negligible toxicity, low cost, and controllability of structural properties of the biosynthesized

75   nanoparticles, thus assuring larger economic and ecological benefits [26]. Plant extracts contain

76   various phytochemicals such as polyphenolic and flavonoids which can reduce metal cations to

77   zerovalent metal nanoparticles and inhibit their agglomeration. In this regard, the extract of

78   several plants such as *Eucalyptus globulus* [27], *Carica papaya*[28], *Nephelium lappaceum L*

79   [29], *Lycopersicon esculentum* [30], and *Corymbia citriodora* [31] has been already studied for

80   the purpose of biosynthesis of ZnO nanoparticles.

81   For the first time, in the current study, we employ the extract of a particular species of

82   *mistletoe* called as *Viscum album* L for biosynthesis of the ZnO-SnO_2 nanocomposite

83   nanoparticles. *Viscum album* L, is one of the evergreen and semi-parasitic plants that grows on

84   different host trees, especially on deciduous trees [32]. This plant is used to treat and prevent

85   various diseases such as diabetes, atherosclerosis, stroke, and hypertension [33]. It shows

86   antiviral, antibacterial, and anti-cancer activities, and thus is widely used as an antioxidant and

87   an immune system regulator [34]. The *Viscum album* extract has been utilized to lower the

88   harmful, mutagenic effects of the radiation-induced oxygen free radicals produced during

89   radiotherapy and chemotherapy [34]. Originating from its phenolic compounds and flavonoids,

90   in this study, the antioxidant activity of *Viscum album's* alcoholic extracts will be quantified.

91   Subsequently, the alcoholic extracts will be used in the biosynthesis of the ZnO/SnO_2 composite

92   nanoparticles that will be later employed for the purpose of photodegradation of Congo red (CR),

93   Biphenyl A (BPA), and tetracycline (TC).

94

95   **2. Materials and methods**

2.1. Preparation of plant samples

Vegetative tissues of *Viscum album* were collected from adult stands of different hosts in Birjand, Iran. The samples were dried and ground, and their extracts were obtained using a soxhlet extraction apparatus (Electro Thermal, UK). To do so, 50 g of the *Viscum album* powder was placed in the soxhlet extraction device and then 500 ml of ethanol, methanol, and acetone were added separately. After 2 h, the extracts corresponding to each alcoholic solvent were separated by centrifugation at 1500 rpm for 15 min and kept in a fridge at 4 ° C.

2.2. Measurement of the phenol content

The Folin-Ciocalteu reagent was applied to evaluate the total amount of phenol. To do so, 5 ml of the Folin-Ciocalteu reagent was added to the extract and the obtained solution was diluted with distilled water and stored in the dark. In the next step, 4 ml of sodium carbonate (Na_2CO_3) was added to the solution and placed in a bain-marie bath in the dark. The phenol concentration was measured by a spectrophotometer at the wavelength of 760 nm. To prepare the standard calibration curve, different concentrations of gallic acid (0, 50, 100, 150, 200, and 250 mg/l) were prepared and their corresponding light absorption intensity was determined [35].

2.3. Measurement of the flavonoid content

Initially, 0.1 ml of aluminum chloride ($AlCl_3$) (10%) and potassium acetate (CH_3CO_2K 1M) were mixed with 2.8 ml of deionized water. In the next step, 0.5 ml of each extract solution was mixed with 1.5 ml of ethanol (96%) and kept at the ambient temperature for 30 min. Then, the absorbance of each compound was calculated at the wavelength of 415 nm by a spectrophotometer. The standard calibration curve was plotted based on different concentrations of quercetin and the amount of flavonoids equivalent to quercetin per mg of each extract was measured.

2.4. Measurement of antioxidant activity

First, 3×10^{-4} DPPH (diphenylpicrylic hydrazyl, 95%) was added to 2.5 ml of the extract ethanol solution. The as-prepared solution was then shaken vigorously for 30 min in the dark at room temperature. Eventually, the absorption intensities were measured at the wavelength of 515

126 nm. The percentage of the entrapped DPPH free radicals, representing antioxidant activity, was
127 calculated using the following equation (1):

$$I\% = [(A_{blank} - A_{sample})/A_{blank}] \times 100 \qquad (1)$$

129 A_{blank}: Absorption of the control sample (without the plant extract)

130 A_{sample}: Sample absorption

131

2.5. Synthesis of the ZnO nanoparticles

133 To prepare the ZnO nanoparticles, first, 1 mM zinc nitrate [Zn $(NO_3)_2.6H_2O$] (with chemical
134 purity of 98%) was dissolved in 50 ml of distilled water and stirred for 1 h. Afterwards, 20 ml of
135 NaOH (96%) solution was added dropwise to the zinc nitrate solution. Eventually, 26 ml of the
136 *Viscum album* extract was included in the final solution that was later stirred for 3 h until it
137 turned yellowish, indicating the formation of the ZnO nanoparticles. The resulting precipitate
138 was centrifuged at 8000 rpm for 15 min and then dried at 70 ° C for 4 h [36].

139

2.6. Synthesis of the SnO$_2$ nanoparticles

141   For the preparation of the SnO$_2$ nanoparticles, 2 g of tin chloride (SnCl$_2$ 2H$_2$O, 98%) was
142 added to 43 ml of the *Viscum album* extract solution. The as-prepared solutions were placed in a
143 water bath at 60 ° C, and subsequently calcined for 60 min at 400 ° C. At the end, a dark gray
144 material remained which was eventually pulverized [37].

145

2.7. Synthesis of the ZnO/SnO$_2$ nanoparticles

147   To prepare the ZnO-SnO$_2$ composite nanoparticles with a 1:1 molar ratio, 0.1 ml of zinc
148 nitrate [Zn(NO$_3$) 2.6H$_2$O, 98%] was mixed with 50 ml of the *Viscum album* alcoholic extract and
149 then 1 ml of NaOH was added dropwise to the solution to adjust the pH at 7. After stirring for 2
150 h, 100 ml of 0.02 M tin chloride [SnCl$_2$. 2H$_2$O, 98%] was added to the solution and stirred for
151 another 2 h at 80 °C. The final solution was then centrifuged and the washed with distilled water
152 and ethanol, and dried in an oven at 80 °C for 4 h. Eventually, the nanoparticles were calcined at
153 800 °C for 1 h [22].

154

2.8. Characterization of the composite nanoparticles

The crystalline structure of the nanoparticles was determined by X-ray diffraction Rigaku MiniFlex 600 (XRD) using Cu-Kα radiation (λ = 0.15418 nm). Fourier transform infrared (FTIR) spectra of the composite nanoparticles were determined by scanning at 400–4000 cm^{-1} (Shimadzo, FT_IR1650 spectrophotometer, Japan). Elemental analysis was carried out using an energy dispersive X-ray spectrometer (EDS) coupled with FESEM. The UV-Vis (DRS) spectra of the samples were determined by a UV-Vis spectrophotometer (Shimadzu, UV-2550, Japan). The morphology of the nanoparticles was monitored using a Field Emission Scanning Electron Microscopy (FESEM) (TE-SCAN, MIRA3 FESEM model). Particle size distribution of the nanoparticles was determined via Dynamic Light Scattering (DLS) using Zetasizer 3000HS. X-ray photoelectron spectroscopy was performed using (XPS VG, Esca Microprob 2000 quantum physical electrons, using Al Ka radiation) to chemically analyze the samples. The size and structure of the nanoparticles were precisely characterized via the TEM analysis (Philips EM208S 100KV).

2.9. Photocatalytic degradation experiments

Photocatalytic activity the composite nanoparticles was employed for the purpose of degradation of Congo red (CR), Bisphenol A (BPA), and tetracycline (TC). To do so, a 350 W xenon lamp (λ> 420 nm) with the intensity of 34.8mW cm^{-2} was used as the solar light simulator source and placed 15 cm away from the reactor. 15 mg of the photocatalyst was mixed with 30 ml of the aqueous solutions containing the mentioned pollutants (20 mg/l). The pH of the solutions was adjusted by adding HCl and NaOH (0.1 mM). In this experiment, an aeration pump and magnetic stirrer were used to supply oxygen in the solution. Prior to irradiation, the solution was homogenized in the dark for 30 min to obtain a stable suspension (achieving a balance between the pollutant solution and the photocatalyst). The effect of temperature (15, 25, 35 and 45 °C), pH (2, 6, 4, 7, 9 and 11), catalyst dosages (0.1, 0.3, 0.5, and 1 g/l), and initial concentrations of pollutants (5, 10, 20, 30, and 40 mg/l) was evaluated. After irradiation for a given time (5, 10, 15, 30, 60, 90, and 120 min), 5 ml of the suspension was removed from the reactor and centrifuged at 4500 rpm for 15 min to separate the catalyst. The final concentration of the pollutants was analyzed by a spectrophotometer at the wavelengths of 502, 227 and 357 nm for CR, BPA and TC, respectively. The photodegradation efficiency of the composite nanoparticles for CR, BPA and TC was calculated using the following equation (2) [38]:

6

$$Removal\ (\%) = (\frac{C_0 - C_t}{C_0}) \times 100 \tag{2}$$

Where, C_0 and C_t are the initial and momentary concentration of CR, BPA and TC, respectively. The amount of total organic carbon (TOC) was also measured by a Schimadzu TOC-Total Organic Carbon Analyzer [39].

2.10. Statistical analysis

Three replicas were used for each measurement to evaluate the reproducibility of the obtained data that were subsequently analyzed using the SPSS software. Statistical differences between the control and treated samples were identified via the one-way analysis of variance (ANOVA) and the Student-Newman-Keuls test. The difference was statistically meaningful when $p < 0.05$.

3. Results and discussion

3.1 Antioxidant activities

The phenolic compounds of a series of plants (such as Plums, kiwi, Black grapes, Artemisia leaves, Rhubarb, Parsley, among others) show antioxidant effect and thus are vital for diet and medicine [40]. Such pharmaceutically active compounds include caffeic, ferulic, chlorogenic acid, and coumarin acid [41, 42]. The phenolic content of the *Viscum album* alcoholic extracts is shown in Table 1.

Table 1. The amount of the phenolic and flavonoid compounds in the alcoholic extracts of *Viscum album*

| The extract solvent	phenolic compounds (mg GAE/g dry sample)	flavonoid compounds (mg QE /g dry sample)
ethanol	21.26 ±0.003	22.36 ±0.45
methanol	23.51 ±0.002	19.38 ±0.35
acetone	18.79 ±0.002	15.79 ±0.5

As can be seen in table 1, the largest amount of phenolic compounds belongs to the *Viscum album* methanol extract (23.51 ±0 0.002 mg/g extract), followed by the ethanol (21.26 ± 0.003 mg/g) and acetone extract (18.79 ± 0.002 mg/g). As a fact, alcoholic solvents are able to

212 extract the largest amount of phenolic compounds from the plant extracts [43]. For instance,

213 Katalinic et al. reported that the highest total phenol content of *T. argentea* was found in the

214 acetone extract, followed by methanol extract and then pure water extract [44]. There is also a

215 direct relationship between the amount of the phenolic compounds of the plant extracts and their

216 antioxidant properties. Considering the abundance of the phenol compounds in plants and their

217 notable antioxidant potential, efficient production of plant extracts has been extensively studied

218 [45]. The phenolic compounds of a mistletoe plant act as a hydrogen donor, thereby offering

219 outstanding antioxidant activity [45, 46].

220 Alike phenolic compounds, flavonoids are one of the most abundant natural compounds

221 that are capable of absorbing free radicals [47]. Table 1 shows the total content of flavonoid

222 available in the *Viscum album* alcoholic extracts. According to this table, the highest amount of

223 flavonoid (22.36 ± 0.45 mg QE/g) is found in the ethanol extract, followed by the methanol

224 (19.38 ± 0.35 mg QE/g) and acetone extract (15.79 ± 0.5 mg QE/g), respectively.

225 The antioxidant compounds of plants such as flavonoids protect their cells against oxidative

226 stress. Flavonoids also show anti-inflammatory, anti-diabetic, and anti-viral properties [48].

227 Under oxidative stress, these compounds attach to membrane phospholipids via hydrogen

228 bonding and accumulate on the internal and external areas of the membrane and protect it [49].

229 Figure 1 shows the scavenging activity of the extracts reflected in their DPPH free

230 radicals inhibition degree. In these measurements, ascorbic acid was used as the control. As can

231 be seen in this Figure, the density of free radicals declines with increasing the concentration of

232 the extract. The highest free radical scavenging activity was achieved by the ethanol extract

233 (83%) and the lowest by the acetone (64%). The free radical scavenging activity of the methanol

234 extract was 75%. Among the alcoholic extracts, the ethanol extract with the concentration of 50

235 μg/ml showed the best results, therefore it was based for the main experiments.
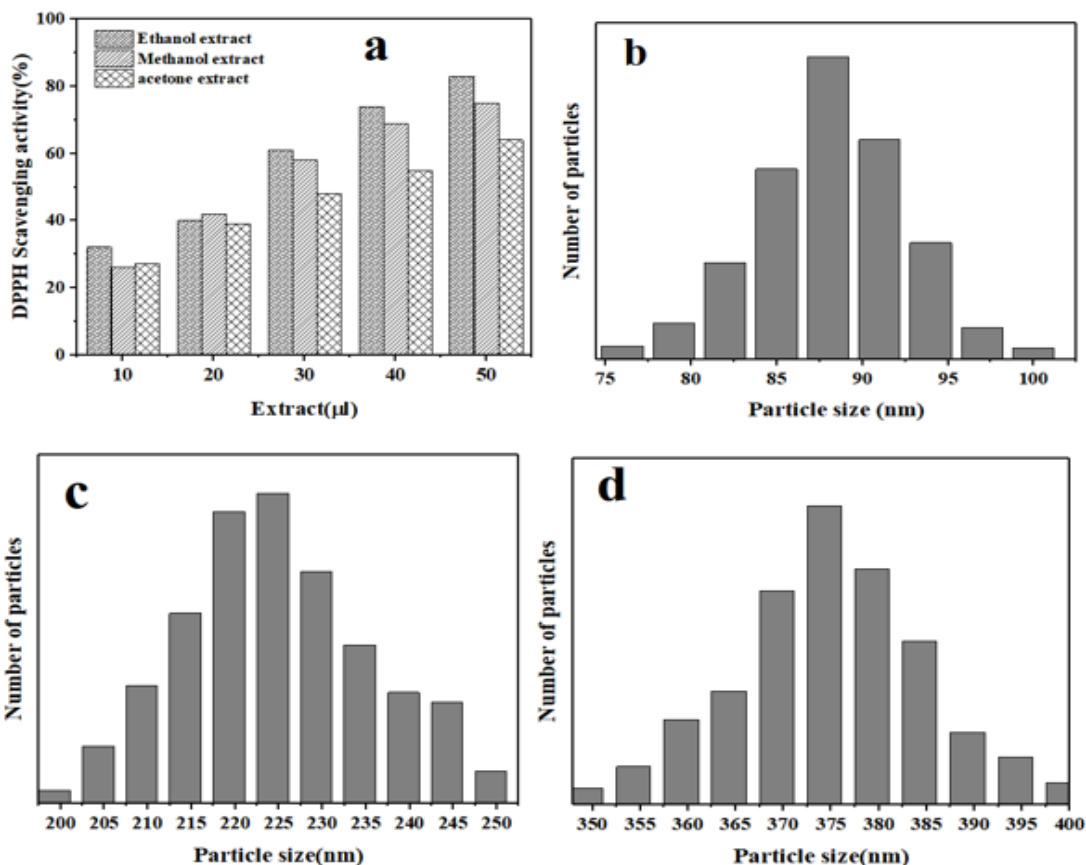
Fig 1. a) DPPH scavenging activity of the alcoholic extracts of *Viscum album*, Particle size distribution of the ZnO/SnO$_2$ nanoparticles synthesized using: b) ethanol, c) methanol, and d) acetone extracts of *Viscum album.*

To calculate the extract concentration providing 50% inhibition (IC$_{50}$), the inhibition power calibration curve (I%) versus the extract concentration (μg/ml) was constructed. According to this curve, IC$_{50}$ for the ethanol extract was determined to be 154.64 μg/ml. Larger extract concentrations provide a higher number of electrons for inactivation of free radicals and thus a more profound inhibitory effect [50].

Table 2. Mean absorbance and IC$_{50}$ values of free radicals in the alcoholic extracts of *Viscum album*

Variables	Degrees of freedom	Sum of squares	Average of squares	The value of F test
The amount of extract consumed	5	0.895	0.179	84.71

9

Error	12	0.0304	0.0025
Total	17	0.9254	

248

3.2. Characterization of the ZnO/SnO$_2$ nanoparticles

3.2.1. Particle size distribution

The DLS analysis indicated that among the nanoparticles synthesized using the three alcoholic extracts, those biosynthesized using the ethanol extract were smallest and almost monodisperse (a low polydispersity index) (Fig. 1b-c). The smaller the particle size, the higher the photoabsorption intensity and thus the photodegradation efficiency is. As seen in Fig. 1a, the nanoparticles derived from the ethanol extract are as small as less than 100 nm and relatively monodisperse, thereby providing uniform photocatalytic properties with high efficiency [3]. Recalling the most optimum scavenging activity of the ethanol extract and also the uniform small size of the nanoparticles biosynthesized using this type of extract, the photodegradation efficiency tests were conducted using these nanoparticles. It is worthy to note that ethanol is one of the most widely used organic solvents for the preparation of plant extracts. It dissolves a wide range of materials, is low cost and eco-friendly, and shows relatively low toxicity [50].

3.2.2. Crystallinity

The XRD patterns of ZnO, SnO$_2$ and ZnO/SnO$_2$ nanoparticles are shown in Fig. 2a. According to these spectra, the crystalline structure of ZnO is hexagonal with characteristic peaks at 2Θ of 31.81°, 34.63°, 36.35°, 47.52°, 56.74°, 62.55°, and 68.10° which correspond to the crystalline planes of (100), (002), (102), (110), (103), (112) and (201), respectively (JCPDS # 00-036- 1451) [22]. With respect to the ZnO/SnO$_2$ nanoparticles, additional peaks appear at 2Θ of 26.65°, 34.62°, 37.90°, 51.37°, 53.55°, 57.82°, 65.78° and 78.85°, which are attributed to the SnO$_2$ crystalline planes of (110), (002), (111), (211), (220), (002), (301) and (321), respectively (JCPDS # 00-041-1445). The diffraction patterns of both ZnO and SnO$_2$ notably changed in the composite nanoparticles in terms of phases and peak positions. However, co-existence of the XRD peaks related to ZnO and SnO$_2$, though with a minor loss of intensity, confirmed the successful formation of a heterojunction between the two metal oxides.

Comparing the full-width half-maximum of the characteristic peaks of SnO$_2$ in the pure and composite form, it can be concluded that the mean grain size of SnO$_2$ declines after

277 hybridization. On the other hand, the diffraction peaks of ZnO nanocrystals in the ZnO/SnO$_2$

278 sample remain intact, though with a lower intensity, implying the presence of highly crystalline

279 ZnO in the nanocomposite nanoparticles.

280 Crystallite size generally correlates with the coherent volume in the material for the

281 respective diffraction peak. Scherrer's equation is applied for determination of the crystallite size,

282 as following:

283 $$D = \frac{0.98\lambda}{\beta\cos\theta}$$ (3)

284 Where D is the crystallite size, λ is the X-ray wavelength, B is the full width at half the

285 maximum (FWHM) and θ is in accordance with peak position. According to the above

286 mentioned equation, the crystallite size of the biosynthesized nanocomposite nanoparticles was

287 calculated to be 48.15 nm.

288

289

11
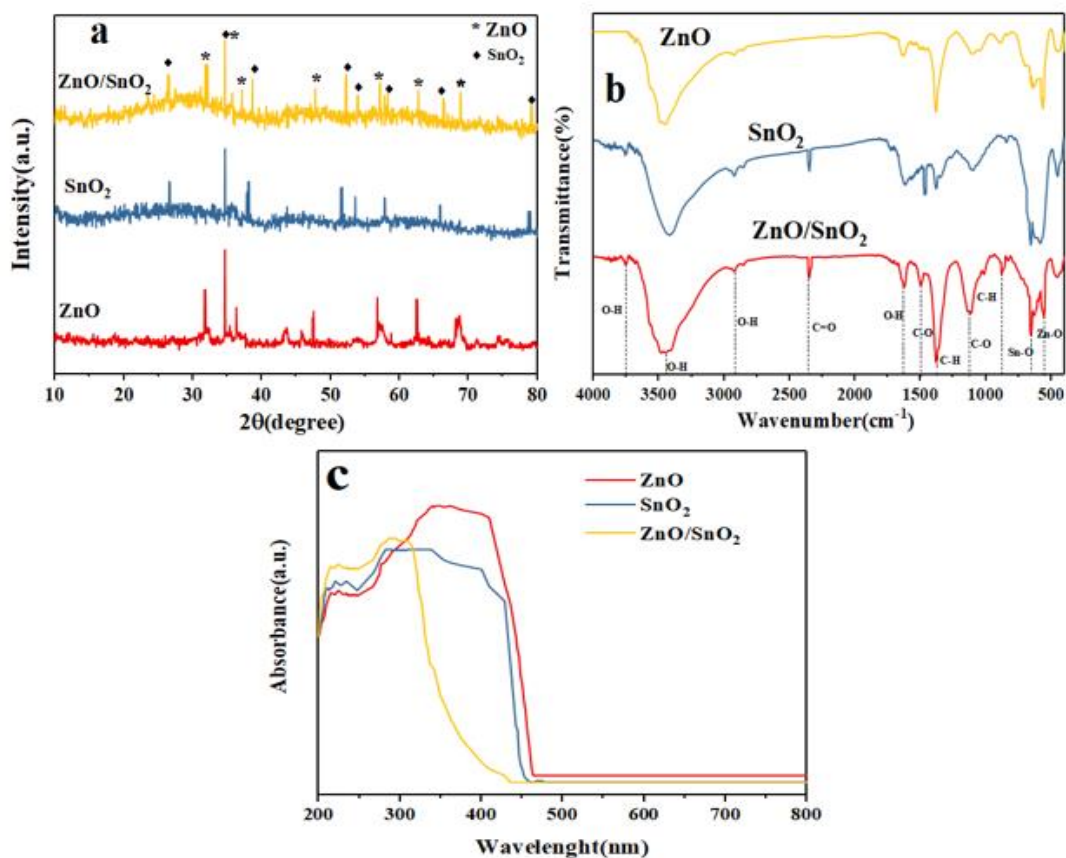
Fig 2. a) XRD, b) FTIR, and c) UV-Vis (DRS) absorption spectra for the photocatalytic nanoparticles made of ZnO, SnO$_2$, and ZnO/SnO$_2$

3.2.3. Surface Chemistry

The FTIR spectra of the biosynthesized ZnO, SnO$_2$, and ZnO/SnO$_2$ nanoparticles are shown in Fig. 2b. With respect to ZnO, tensile vibration of the Zn-O bond is reflected at the peak located at 555 cm^{-1} [51]. The absorption peak at 3431 cm^{-1} is attributed to the OH tensile vibration mode. The absorption peaks located below 2000 cm^{-1} including the one at 1634 cm^{-1} emerge due to the bending vibrations of molecular water adsorption. Regarding SnO$_2$, the peak at 659 cm^{-1} is attributed to the Sn-O tensile vibration [52]. On the other hand, the peaks appearing at 1105 and 1462 cm^{-1} are assigned to the tensile vibration of O–C due to the presence of *Viscum album* extracts [52, 53]. The peaks at 2347, 1380, and 875 cm^{-1} are attributed to the symmetrical tensile vibrations of C=O and C-H [54]. The peaks at 2934 and 3740 cm^{-1} are related to the O-H tensile vibration. These results imply the presence of the organic phase of the *Viscum album* extract as well as successful biosynthesis of ZnO and SnO$_2$ for samples.

3.2.4. Optical properties

The optical properties of the biosynthesized nanoparticles were characterized via UV-Vis spectroscopy. Fig. 2c displays the UV-Vis (DRS) absorption spectra for the ZnO, SnO$_2$, ZnO/SnO$_2$ nanoparticles. As can be seen in the figure, ZnO nanoparticles show a sharp increase in the absorption intensity within the UV region. In the case of SnO$_2$, increase in the UV absorption intensity is correlated to electron transition between the valence band (VB) and the conduction band (CB), and is known as the optical absorption edge. The highest UV light absorption intensity belonged to ZnO nanoparticles. The UV absorption edge of the ZnO/SnO$_2$ nanoparticles gradually declined and shifted to the visible light area due to the insignificant crystallization of these nanoparticles. The occurrence of the absorption edge at higher wavelengths implies that these heterogeneous composite nanoparticles can offer an improved photocatalytic activity when excited by visible light [5, 55].

3.2.5. Surface chemical composition

The surface chemistry of the ZnO/SnO$_2$ composite nanoparticles was studied by XPS analysis. The XPS spectra validated the presence of O, C, Sn, and Zn. According to Fig. 3a, the

321   Zn and Sn peaks are evident in the high- resolution spectrum of the composite nanoparticles. The

322   peaks emerging at 1020.6 eV and 1044 eV, Fig. 3b, correspond to Zn 2p3/2 and Zn 2p1/2 [3, 51].

323   The peaks seen at 486.3 eV and 494.4 eV, Fig. 3c, can be assigned to Sn3d5/2 and Sn3d3/2 Sn

324   (IV), respectively, which point out to the coupling energy of Sn^{4+} ion in SnO_2 [56]. The O1

325   spectrum is characterized by the energy coupling peaks at 530.2, 530.7 and 531.5 eV, Fig. 3d. In

326   this spectrum, the coupling peaks appearing at 530.2 eV and 530.7 eV are attributed to oxygen at

327   the Sn-O and Zn-O bonds, respectively [57, 58].

328

329

330

13
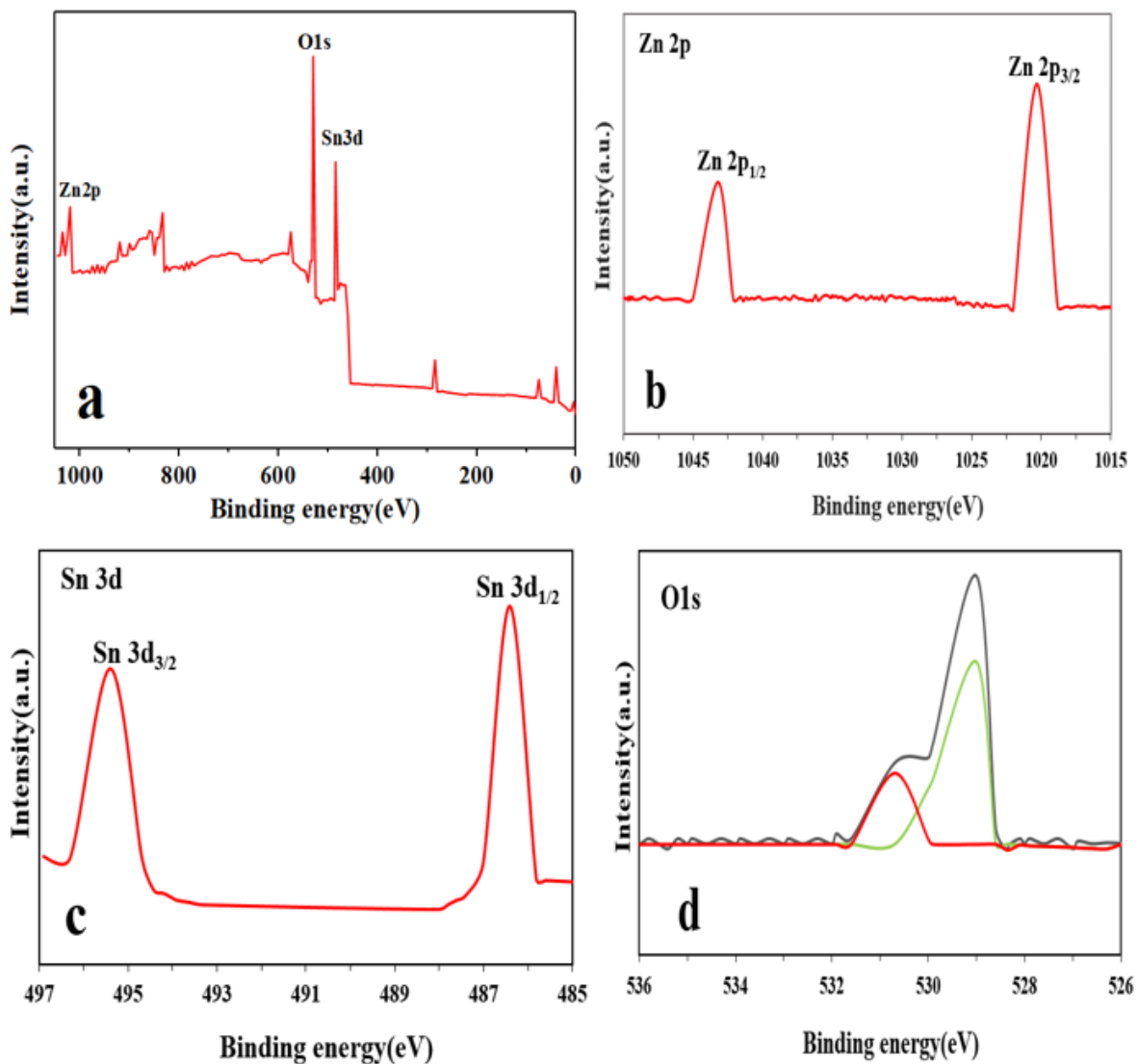
Fig 3. XPS analysis of the ZnO/SnO$_2$ biosynthesized nanoparticles: (a) general XPS spectrum, (b) Zn2p, (c) Sn3d, and (d) O1s spectrum of the composite nanoparticles.

3.2.6. Morphological characteristics

Fig. 4a-c shows the FESEM images of the ZnO/SnO$_2$ biosynthesized nanoparticles. The nanoparticles are uniform and spherical. These images show that using the extract as a surfactant leads to formation of the nanoparticles with larger sizes in an almost monodisperse manner. The nanoparticles are aggregated most likely due to heterogeneity of the their suspensions before imaging [5, 59].
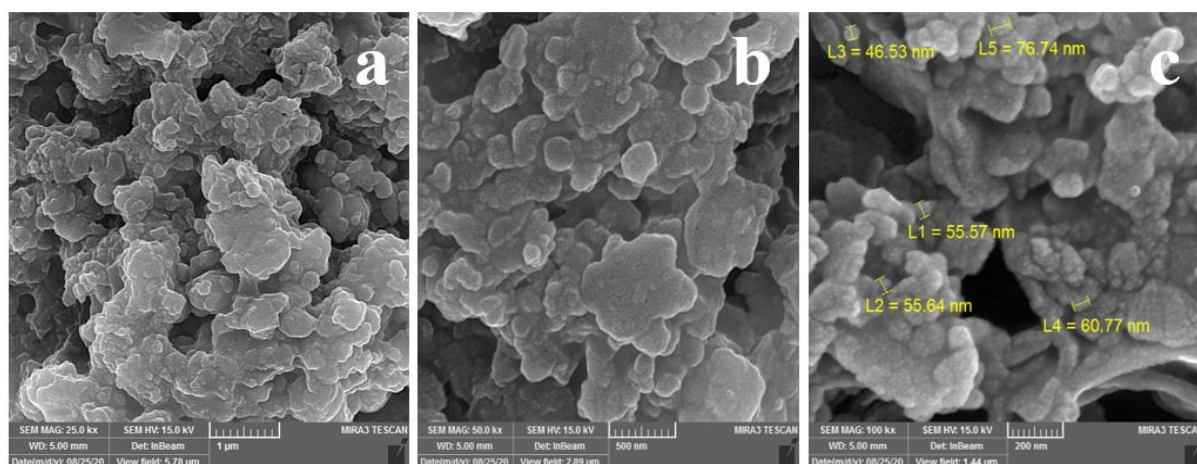
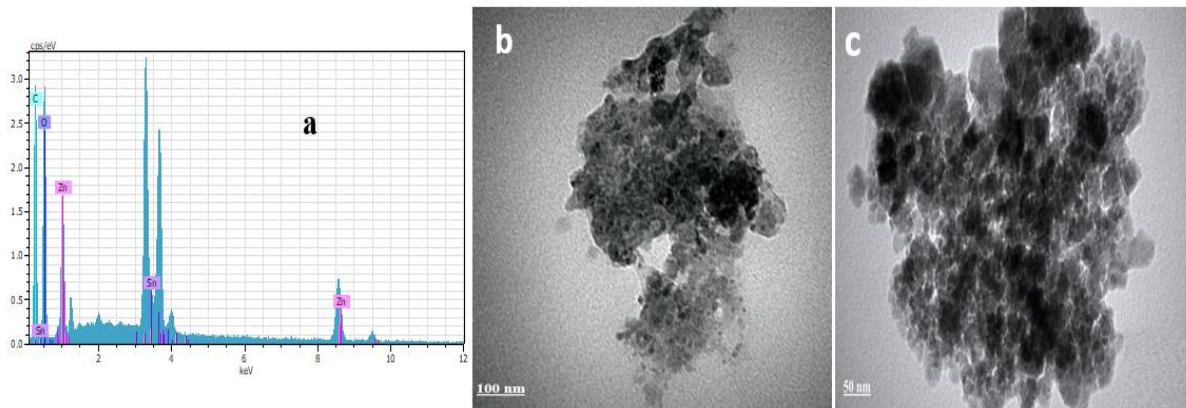**Fig 4.** FESEM images show the biosynthesized ZnO/SnO$_2$ nanoparticles at different magnifications (scale bars represent 1μ (a), 500 nm (b) and 200 nm (c), respectively).

Energy dispersive spectroscopy (EDS) analysis was successful in validation of the presence of Zn, Sn, O, and C in the ZnO/SnO$_2$ nanoparticles. The carbon and oxygen originate from the phenolic compounds of the remaining *Viscum album* extract, Fig. 5a. Fig. 5b and c show TEM images of the ZnO/SnO$_2$ nanoparticles at different magnifications. As seen in the TEM images, spherical nanoparticles are fused to each other, forming clusters made of ZnO/SnO$_2$.

Fig 5. a) EDS spectrum and (b) TEM images of the biosynthesized ZnO/SnO$_2$ composite nanoparticles.

3.3. Photodegradation of the organic pollutants

3.3.1. Photolysis and adsorption

To conduct the photolysis experiments, the pollutant (CR, BPA, and TC) containing aqueous solutions (10 mg/l and pH7) were irradiated with a Xenon lamp for 1 hr. In the case of adsorption measurements, the above conditions were repeated, while adding the composite nanoparticles. The adsorption extent of the ZnO/SnO$_2$ nanoparticles (q_t) was determined at various time intervals through the following equation (4) [60]:

$$q_t = \frac{(C_O - C_t)V}{m} \qquad (4)$$

Where C_0 is the initial concentration of the pollutant and C_t is the concentration of the pollutant at time t (mg/l). V is the volume of the CR, BPA and TC pollutants containing solutions (ml) and m is the mass of the ZnO/SnO$_2$ nanoparticles (mg). The equilibrium adsorption capacity of the ZnO/SnO$_2$ nanoparticles, q_e (mg/g) was measured via the following equation (5) [60]:

$$q_e = \frac{(C_O - C_e)V}{m} \qquad (5)$$

Where C_0 and C_e are the initial and equilibrium concentration of the pollutant (mg/l), respectively. V is the bulk volume of the pollutant containing aqueous solution (ml) and m is the mass of the ZnO/SnO$_2$ nanoparticles (mg). As shown in Fig. 6a, degradation percentage of the organic pollutants, i.e., CR, BPA, and TC, due to photolysis was 13.08%, 10.61%, and 8.4%, respectively. These results match well with those reported by Rosenfeldt et al. [61] and Garg et

al. [60] implying that photolysis of BPA by short time light irradiation was negligible. On the other hand, removal percentage of the organic pollutants by the ZnO/SnO_2 nanoparticles in the dark solely due to adsorption was 26.55%, 23.64%, and 20.87%, for CR, BPA, and TC, respectively.
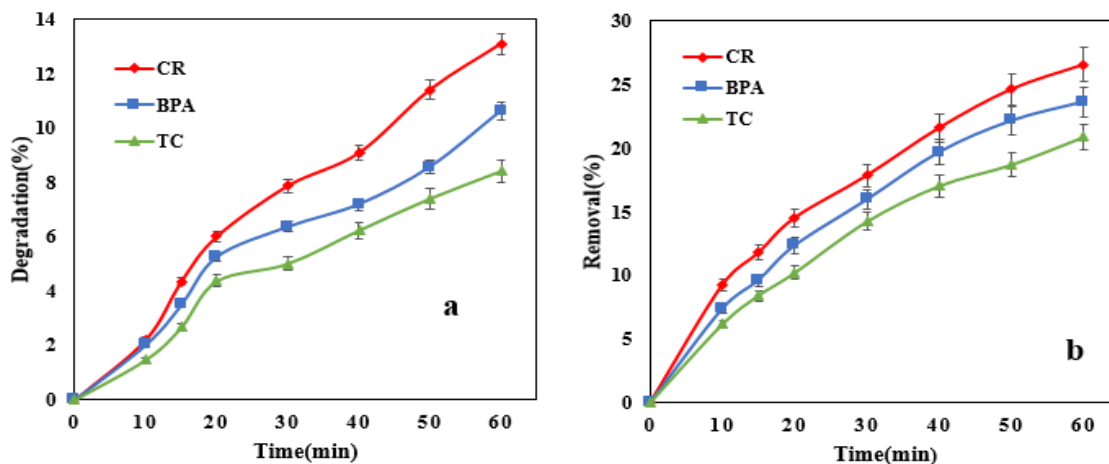
Fig 6. (a) Photolysis and (b) adsorption behavior of CR, BPA, and TC on the ZnO/SnO_2 nanoparticles.

3.3.2. Photodegradation analysis

The solar light induced photocatalytic activity of the biosynthesized nanoparticles of ZnO, SnO_2 and ZnO/SnO_2 in the presence of the studied organic pollutants is demonstrated in Fig. 7. As shown in this figure, photodegradation percentage of CR, BPA, and TC by the ZnO/SnO_2 nanoparticles is significantly higher compared to that by the ZnO and SnO_2 nanoparticles alone. SnO_2 possesses electrons with higher mobility away from the valence band towards the entrapping surfaces, thus can act as electron storage and create more electron and hole pairs to produce hydroxyl radicals [3]. In other words, coupling of ZnO and SnO_2 leads to an increase in the electron transfer rate through the interface and prevents the recombination of electrons and holes, thereby enhancing the photocatalytic activity of the ZnO/SnO_2 nanoparticles.

16

391
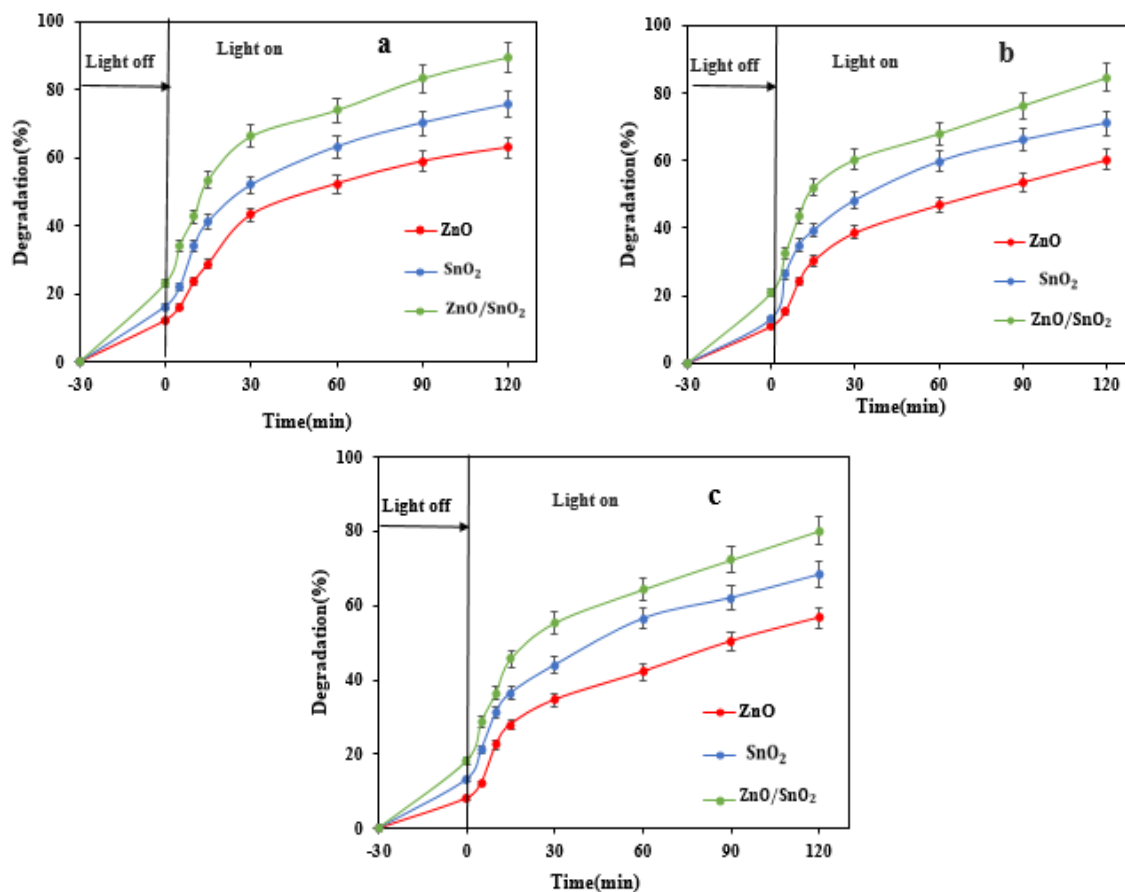
Fig 7. Comparison of the photodegradation efficiency of the ZnO, SnO$_2$ and ZnO/SnO$_2$

biosynthesized nanoparticles for: a) CR, b) BPA and c) TC.

394

3.3.3. The effect of the photocatalyst dosage

To determine the effect of the photocatalyst dosage on photodegradation of the organic pollutants, different dosages of photocatalysts (0.1, 0.3, 0.5, 0.7 and 1 g/l) were employed and their contribution to removal of CR, BPA and TC was explored. The other experimental conditions included: pH7, 10 mg/l initial concentration of the pollutants and temperature of 25°C. As shown in Fig. 8, after 2 hr (120 min) irradiation, based on the photocatalyst dosage of 0.5 g/l, the highest photodegradation efficiency for CR, BPA, and TC was measured to be as large as 88.14%, 85.82%, and 81.39%, respectively. There is an increasing trend for the photodegradation efficiency with the photocatalyst dosage up to 0.5 g/l. The larger the photocatalyst dosage, the higher the light absorption intensity and the number of active sites and thus the higher pollutant removal rate will be [62-64]. However, over this critical dosage,

406   photodegradation efficiency drops, most likely due to turbidity of the solution being treated.

407   Turbidity hampers light penetration into the solution and thereby hinders the generation of

408   reactive OH radicals that are responsible for photodegradation of the organic pollutants. The

409   other reason for loss of the photodegradation efficiency at high photocatalyst dosages could be

410   aggregation of the nanoparticles that reduces the number of the available active sites.

411
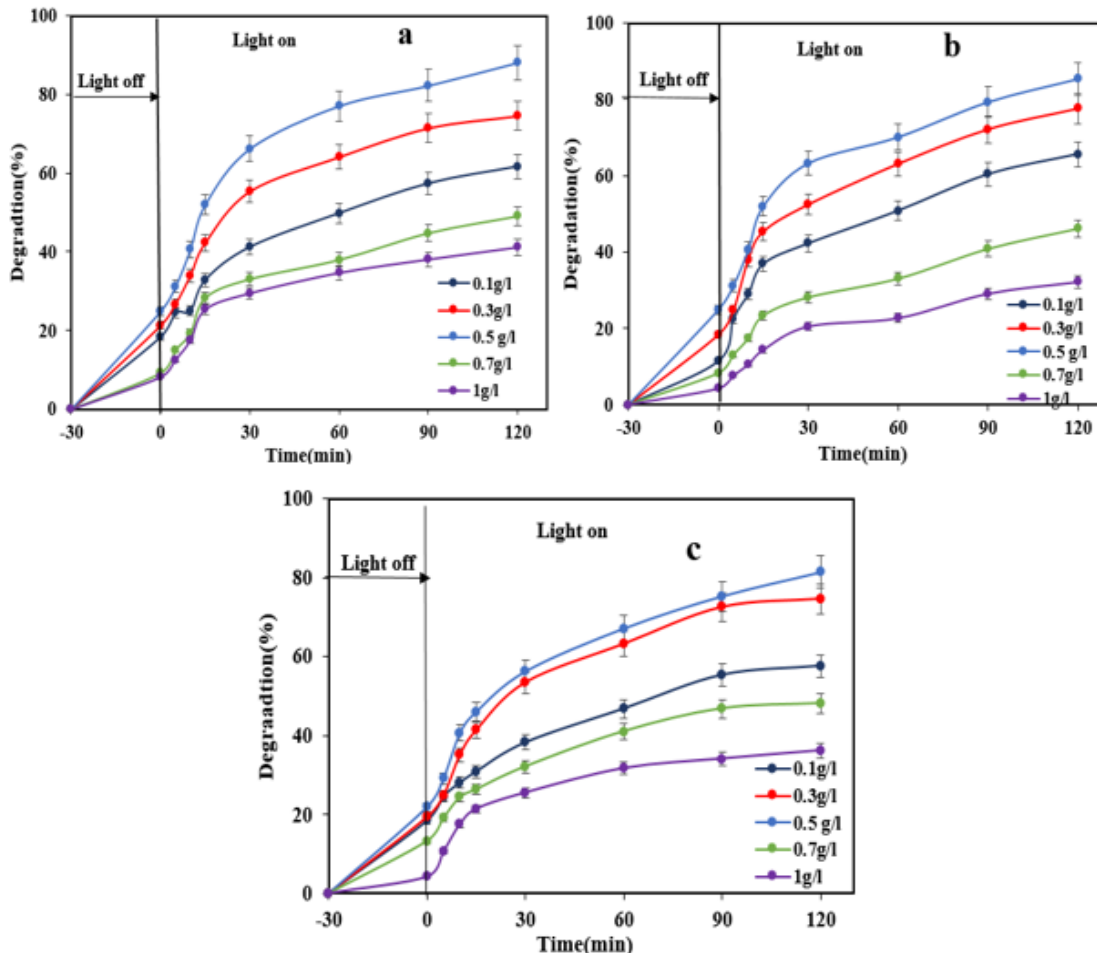
413   **Fig 8.** The relationship between the photocatalyst dosage and photodegradation efficiency for: a)

414   CR, b) BPA and c) TC.

415

416   **3.3.4. The effect of pH**

417   The photocatalytic reactions are mediated by pH, organic pollutant content, and

418   adsorption capacity of the photocatalyst surface [62]. Therefore, pH plays a vital role for

419   efficient photodegradation of organic pollutants. In order to determine the optimum pH required

18

420 for removal of CR, BPA, and TC, the photodegradation experiments were performed under a
421 fixed concentration of the pollutants (10 mg/l) and the photocatalyst (0.5 g/l), but at different pH
422 values of 2, 4, 6, 7, 9, and 11. As shown in Fig. 9, the highest degradation rate for the three
423 pollutants was achieved under mild acidic conditions and was recorded as 94.25% (for CR at pH
424 6), 87.36% (for BPA at pH4), and 83.76% (for TC at pH4). As verified earlier, pH is the most
425 influential parameter in the degradation process of many biological and chemical substances
426 [65]. Our study showed that the most efficient degradation takes place at the acidic pHs of 4 and
427 6, due to the high concentration of hydroxyl radicals in the solution, which play a significant role
428 in the oxidation of organic pollutants [66]. Also, at acidic pHs, the surface of the biosynthesized
429 nanoparticles (ZnO/SnO$_2$) gets protonated, thus driving an electrostatic interaction with CR,
430 BPA, and TC anionic pollutants [64]. In contrary, at alkaline pHs, anionic CR, BPA and TC are
431 repelled from the hydroxylated surface of the nanoparticles and thus adsorption level remains
432 insignificant. Under acidic conditions, the adsorbed CR, BPA and TC molecules can be readily
433 oxidized by OH radicals created upon light irradiation, leading to their further removal [3].
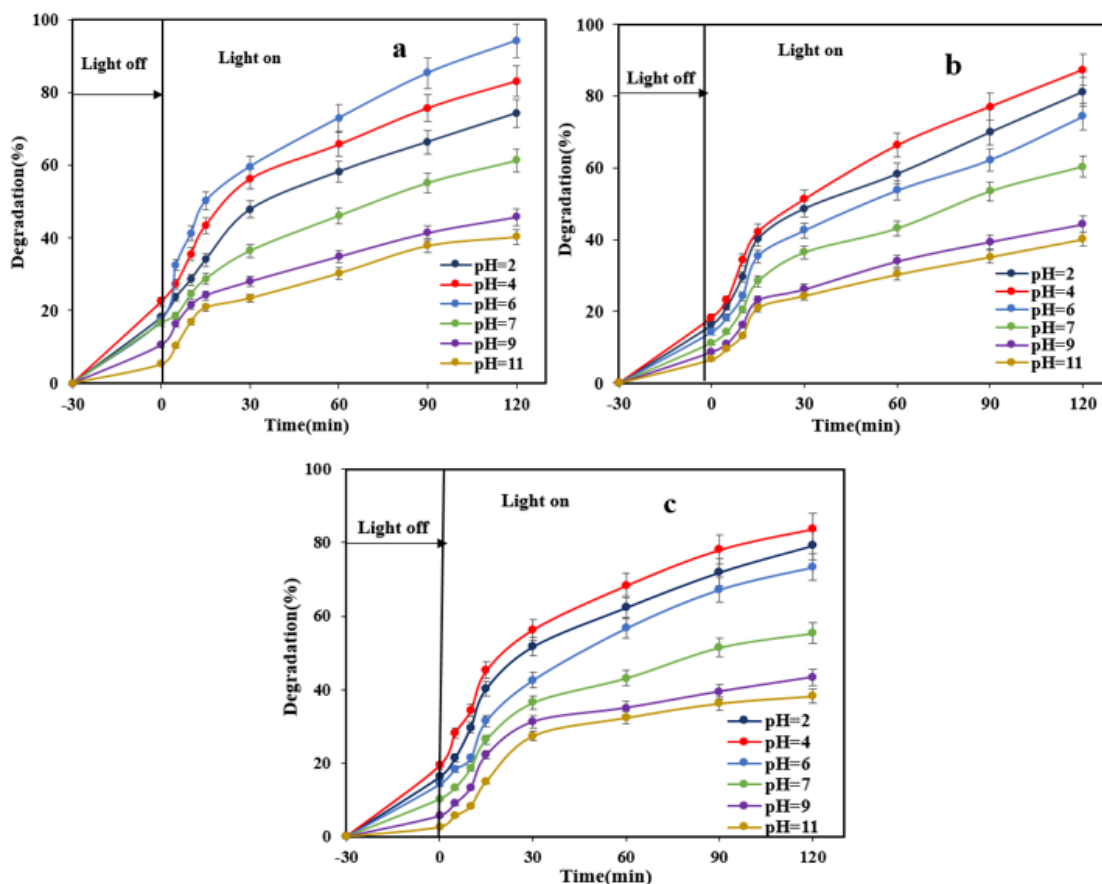

434

435   **Fig 9.** The effect of pH on photocatalytic degradation of: a) CR, b) BPA and c) TC, over a 120

436   min light irradiation cycle.

437

438   **3.3.5. The effect of temperature**

439   The effect of different temperatures (15, 25, 35, and 45 °C) on the degradation level of

440   CR, BPA and TC catalyzed by the composite nanoparticles was investigated. For this

441   experiment, the testing conditions included: catalyst dosage of 0.5 g/l, pollutant concentration of

442   10 mg/l, and optimal pH of 4 for BPA and TC, and of 6 for CR. As shown in Fig. 10, the higher

443   the temperature, the larger the photodegradation efficiency is. Raising the temperature from 15 to

444   45 °C, degradation efficiency increases up to 90.43%, 83.22%, and 85% for CR, BPA and TC,

445   respectively. This improvement stems from this fact that at higher temperatures, a larger number

446   of OH radicals are generated that can notably degrade the organic pollutants.
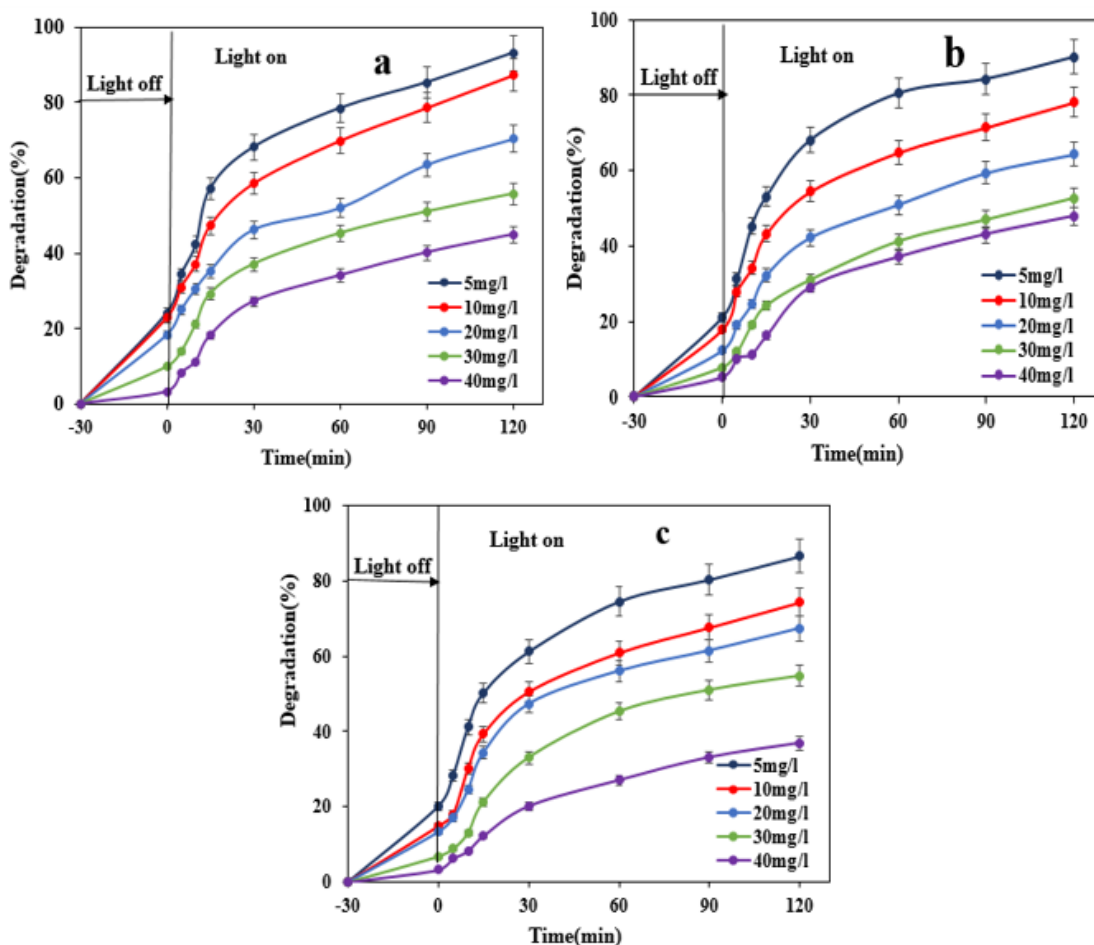
447
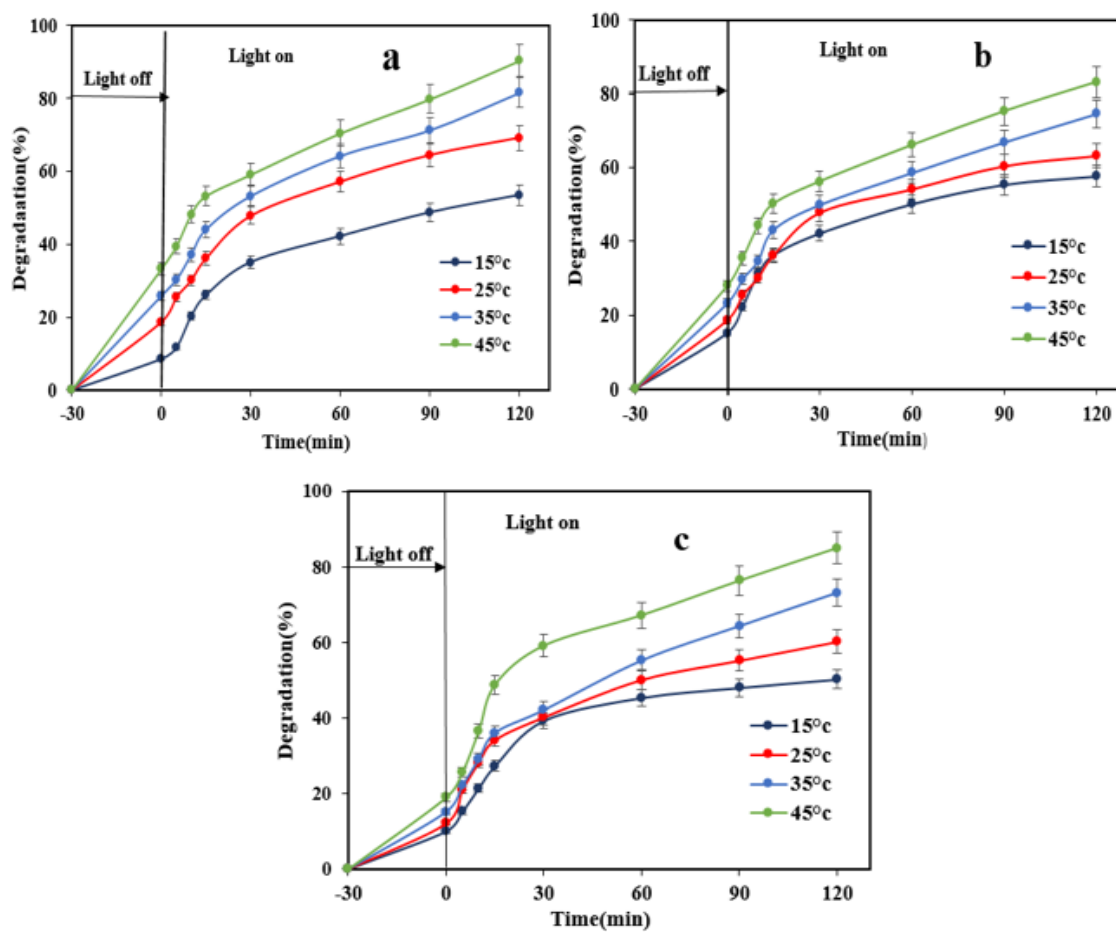
448

449 **Fig 10.** The effect of temperature on photodegradation efficiency of the biosynthesized
450 composite nanoparticles for: a) CR, b) BPA, and c) TC.

451

452 **3.3.6. The effect of initial pollutant concentration**

453   As shown in Fig. 11, photodegradation efficiency for CR, BPA and TC declines with
454 increasing their initial concentration. Regardless of the pollutant type, the highest
455 photodegradation efficiency was obtained at the initial concentration of 5 mg/l and with further
456 increase of the initial concentration, photodegradation efficiency declined. It is assumed that with
457 enhancement of the initial concentration, a larger number of the pollutant molecules sticks on the
458 surface of the photocatalyst, thereby reducing the production of hydroxyl radicals (OH) [59, 67,
459 68]. This loss in the photodegradation efficiency might be also related to blockage of light
460 penetration at higher concentrations of the pollutants and thus generation of a lower density of
461 the reactive radicals [69].

462

463

Fig 11. The effect of the initial pollutant concentration on photodegradation efficiency of the biosynthesized composite nanoparticles for: a) CR, b) BPA, and c) TC.

3.4. Photodegradation kinetics

The photocatalytic degradation of CR, BPA, and TC by the biosynthesized nanoparticles (ZnO/SnO_2) was consistent with the pseudo-first-order kinetic model. The rate constant (K_{app}) of the reactions was determined through the pseudo-first order kinetic equation (6)[5]:

$$\frac{dC}{dt} = -K_{app}C \qquad (6)$$

Where C is the pollutant concentration and t is the reaction time. The equation 5 can be converted to the following equation (7):

$$Ln(\frac{C_0}{C_t}) = K_{app} \times t \qquad (7)$$

Here C_0 and C_t are the initial concentration and momentary concentration of the pollutant, respectively. As shown in Fig. 12a-c, there is a linear relationship between C_0/C_t and irradiation time, implying that degradation of the pollutants (CR, BPA, and TC) follows the pseudo-first-order kinetic model. On the other hand, the regression coefficient and the degree of correlation obtained from Fig. 12a-c confirm that the degradation behavior complies well with the L-H model. The initial reaction rates and constants for photodegradation of CR, BPA, and TC are tabulated in Table 3. As seen in this table, R^2 values were close to 1 but declined with increasing the pollutants rate [5]. In fact, the photodegradation rate decreased with rising the pollutants concentration. As shown in Table 3, it turns out that the photodegradation rate constant reduces with increment of the pollutants concentration, most likely due to formation of intermediate products that neutralize the hydroxyl radicals.
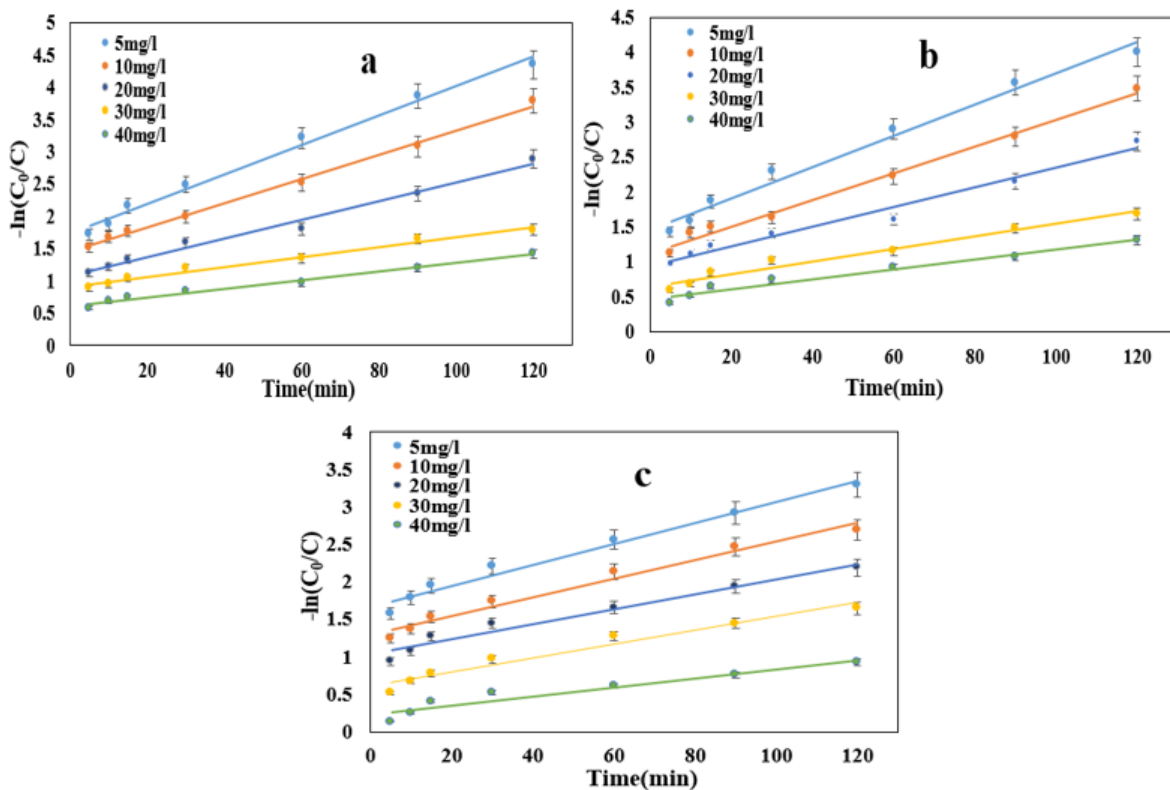
Fig 12. Kinetic plots of the photodegradation process of: a) CR, b) BPA, and c) TC, in the presence of the biosynthesized composite nanoparticles with varying dosages.

Table 3. The first-order kinetic model parameters for the photocatalytic degradation process of the organic pollutants

CR Concentration (mg/L)	Reaction Rate (k) (min^{-1})	Correlation Coefficient (R^2)	Fitting Equation
5	0.0228	0.09891	Y=0.0228x+1.7363
10	0.0189	0.996	Y=0.0189x+1.4455
20	0.0145	0.9848	Y=0.0145x+1.0745
30	0.0078	0.9824	Y=0.0078x+0.9006
40	0.0067	0.9865	Y=0.0067x+0.6009
BPA Concentration (mg/L)	Reaction Rate (k) (min^{-1})	Correlation Coefficient (R^2)	Fitting Equation

23

5	0.0223	0.9831	Y=0.0223x+1.4658
10	0.0192	0.9907	Y=0.0192x+1.1183
20	0.014	0.9762	Y=0.014x+01.9466
30	0.0091	0.9694	Y=0.0091x+0.6376
40	0.0071	0.963	Y=0.0071x+0.4652
TC Concentration (mg/L)	**Reaction Rate (k) (min^{-1})**	**Correlation Coefficient (R^2)**	**Fitting Equation**
5	0.0139	0.978	Y=0.0139x+1.6725
10	0.0124	0.9766	Y=0.0124x+1.2975
20	0.01	0.9640	Y=0.01x+1.0327
30	0.0093	0.958	Y=0.0093x+0.6076
40	0.0006	0.9197	Y=0.0006x+0.2358

493

494   To investigate the mineralization of CR, BPA, and TC pollutants and their optimum

495   photodegradation by the composite nanoparticles, total organic carbon (TOC) value was

496   quantified, Fig. 13. The degradation (removal) of TOC can properly indicate the mineralization

497   of the organic pollutants. The TOC removal in the first 30 minutes of the reaction was about

498   54.23%, 56.78%, and 55.14% for CR, BPA, and TC, respectively. After 120 minutes, the TOC

499   degradation percentage raised up to 78.26%, 80.15%, and 75% for CR, BPA, and TC,

500   respectively.
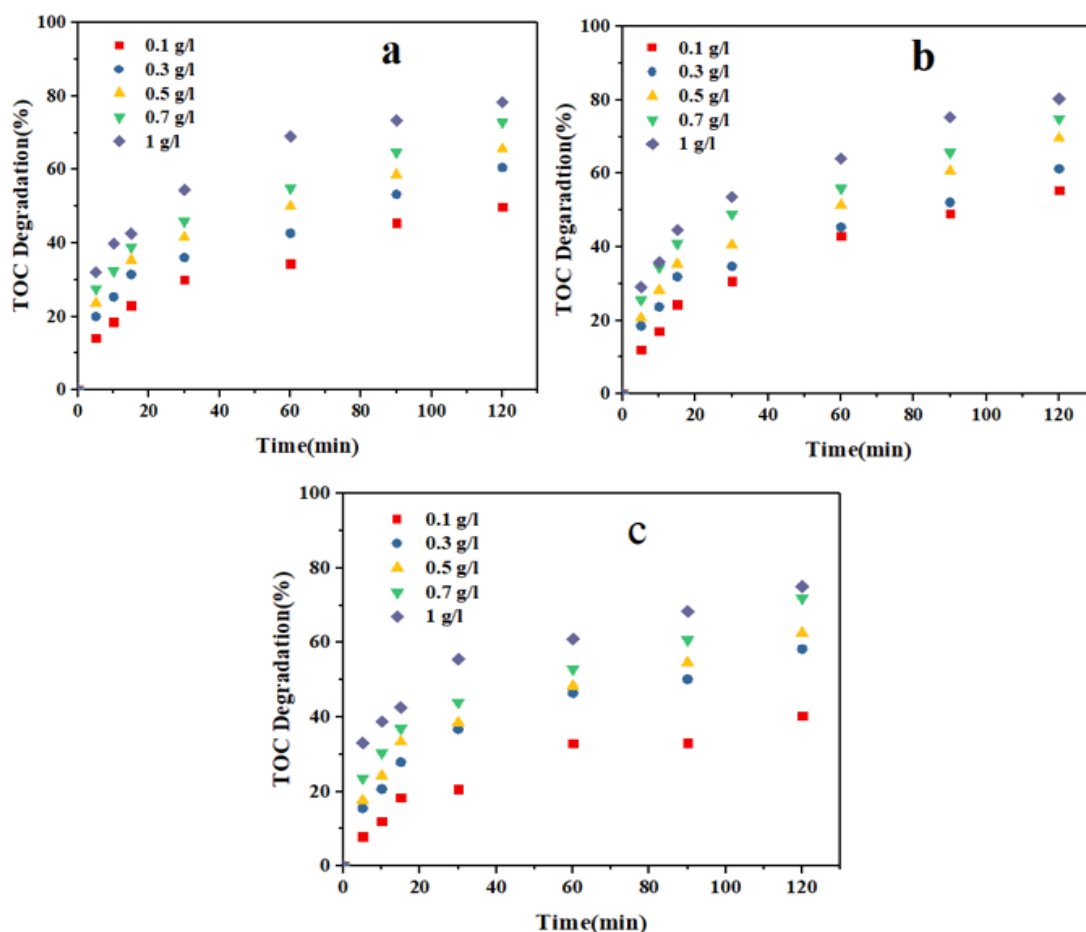
Fig 13. The TOC degradation percentage over the irradiation time for: a) CR, b) BPA, and c) TC.

3.5. Stability and recyclability of the photocatalyst nanoparticles

The recyclability and stability of photocatalysts are crucial for their industrial applications and for wastewater treatment [59]. To determine the reusability of the photocatalyst (ZnO/SnO_2), the photodegradation process was repeated for four successive cycles. To do so, after each cycle, the nanoparticles were collected via filtration and used for a new photodegradation process. As shown in Fig. 14, photodegradation efficiency after four successive cycles declined from 93.44% to 85.36% (CR), from 90.12% to 82.49% (BPA), and from 85.5% to 73.51% (TC). Therefore, it can be confidently stated that the biosynthesized nanoparticles are sufficiently stable and recyclable. The insignificant loss in the photodegradation efficiency might originate from occupation of the surface active sites of the

515   photocatalyst by CR, BPA, and TC molecules, reducing the photogeneration of holes and

516   electrons.

517
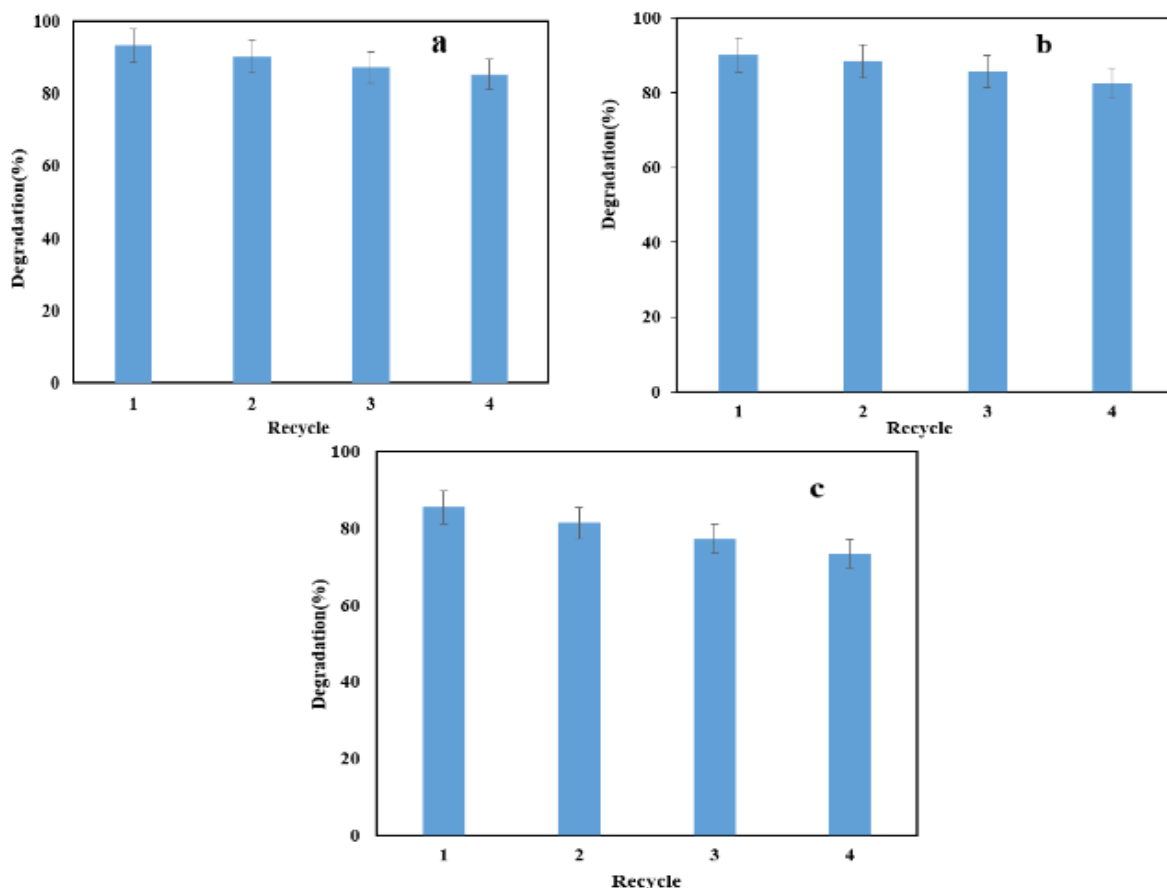
Fig 14. Stability and reusability of the biosynthesized nanoparticles for photodegradation of: a)

519   CR, b) BPA, and c) TC.

520

3.6. Photodegradation mechanism

522   Fig. 15 schematically demonstrates the charge transfer process by the ZnO and SnO_2

523   nanoparticles. When the biosynthesized ZnO-SnO_2 nanoparticles are irradiated, electrons (e^-) are

524   transferred from the ZnO conduction band (CB) to the SnO_2 valence band (VB). The holes also

525   simultaneously shift from the VB of SnO_2 to the VB of ZnO. In other words, supposing that the

526   diversity between the conduction band edge and the flat band potential is insignificant, the ZnO

527   and SnO_2 valence band edges can be found by adding more band gap energy to the flat band

528   potential rate. And since the ZnO band gap energy is lower than that of SnO_2, electrons are

529   shifted from the ZnO's CB to the SnO_2's VB. The photogenerated electrons can react with the

530   molecule of oxygen, and the holes are trapped by OH, resulting in the formation of a •OH radical

531 and a superoxide anion radical (O_2^-). In other words, electrons (e^-) can reduce the molecular

532 oxygen adsorbed on the surface of the photocatalyst creating a superoxide anion ($O_2^{-\bullet}$) and this

533 superoxide anion can further produce •OH radicals through the formation of HOO• radicals and

534 H_2O_2. These radicals are able to oxidize CR, BPA, and TC molecules and thus photodegrade the

535 organic pollutants [70]. Accordingly, effective charge segregation enhances the longevity of

536 charge carriers and decreases the recombination rate of the electron-hole pairs by formation of

537 the Schottky barriers conduction band for trapping electrons and thus improves the

538 photocatalytic potential.

539   The outstanding photocatalytic activity of the ZnO-SnO$_2$ nanoparticles compared to the

540 pure oxides can be attributed to co-existence of two semiconductors with different CB and VB

541 energy levels. Depending on the potentials of the photogenerated electrons (e^-) and holes (h^+),

542 vectorial transfer of charge carriers from a semiconductor to another is realized. As a result,

543 electrons and holes are more efficiently separated and a higher photocatalytic activity is achieved

544 [71]. The ZnO and SnO$_2$ nanoparticles are n-type semiconductors and the difference between the

545 CB edge and the flat band potential is negligible. Therefore, it can be determined the valence

546 band edge of ZnO and SnO$_2$ by adding the bandgap energy to the flat band potential value [22].

547 The VB of the ZnO nanoparticles (E_{VB} = 2.84 eV) is less than that of the SnO$_2$ nanoparticles

548 (E_{VB} = 3.44eV). Similarly, the CB of the ZnO nanoparticles (E_{CB} = -0.36 eV) is inferior to that of

549 the SnO$_2$ nanoparticles (E_{CB} = -0.11 eV), Fig.15. When the ZnO/SnO$_2$ nanocomposites are

550 irradiated by the solar light, electrons (e^-) can shift from the more cathodic CB of ZnO to the

551 more anodic CB of SnO$_2$. Similarly, holes can move from the VB of SnO$_2$ to the VB of ZnO.

552 The effective charge separation can increase the lifetime of the charge carriers and thus promote

553 the interfacial charge transfer to the adsorbed substrates.
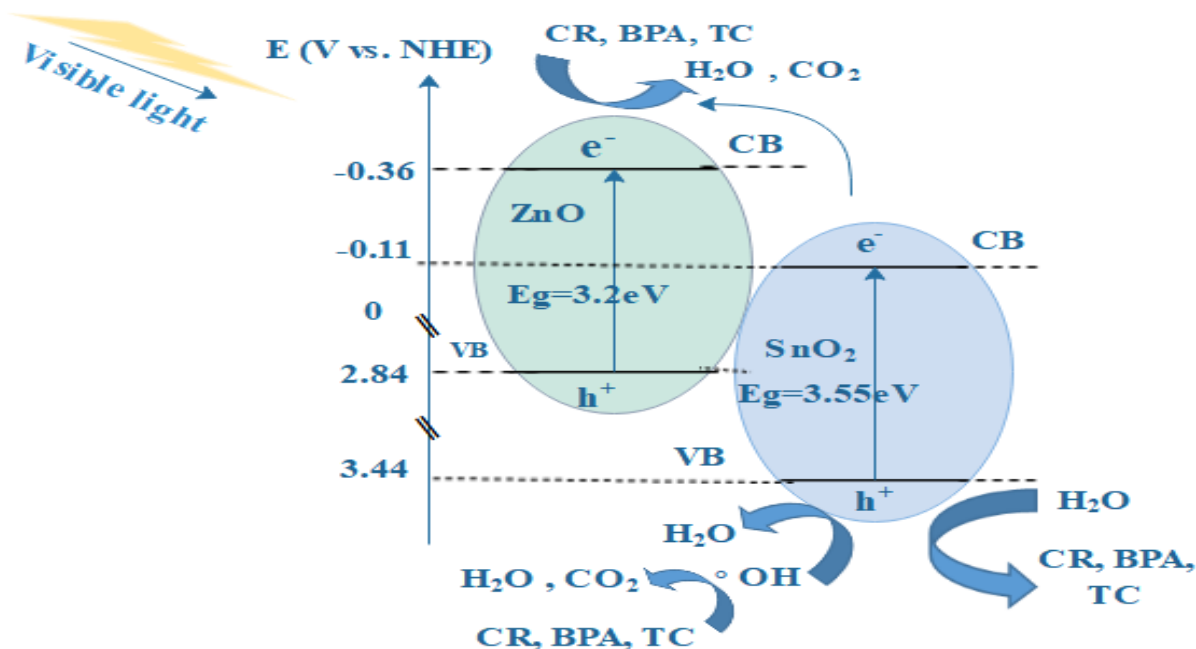
554

555

556

Fig 15. Schematic diagram of the charge transfer routes between the ZnO/SnO$_2$ phases

558

4. Conclusion

In this study, we experimentally validated that the *Viscum album* extract offers outstanding antioxidant properties, thanks to its abundant phenolic and flavonoid compounds. We benefitted from the *Viscum album* alcoholic extract to synthesize the ZnO/SnO$_2$ composite nanoparticles in an eco-friendly manner. The as-synthesized nanoparticles (ZnO/SnO$_2$) were subsequently used for photodegradation of three organic pollutants commonly found in wastewater streams including CR, BPA, and TC. Thanks to exceptional optical properties of the nanocomposite nanoparticles, a high photodegradation efficiency of 93.44% (CR), 90.12% (BPA), and 85.5% (TC) under solar light was achieved. The biosynthesized nanoparticles showed promising stability after 4 reuse cycles and were able to still optimally photodegrade the organic pollutants. Conclusively, the biosynthesized photocatalytic nanoparticles can be used as a promising material that can remove organic pollutants from wastewater in a sustainable and energy efficient way.

Conflicts of interest

There are no conflicts to declare.

574

28

579

580   **References**

581   [1] M. Palaniappan, P.H. Gleick, L. Allen, M.J. Cohen, J. Christian-Smith, C. Smith, N. Ross, Clearing the
582   waters: a focus on water quality solutions, 2010.
583   [2] M. Pera-Titus, V. García-Molina, M.A. Baños, J. Giménez, S. Esplugas, Degradation of chlorophenols
584   by means of advanced oxidation processes: a general review, Applied Catalysis B: Environmental 47(4)
585   (2004) 219-256.
586   [3] N. Ahmadpour, M.H. Sayadi, S. Sobhani, M. Hajiani, A potential natural solar light active
587   photocatalyst using magnetic $ZnFe_2O_4@ TiO_2/Cu$ nanocomposite as a high performance and recyclable
588   platform for degradation of naproxen from aqueous solution, Journal of Cleaner Production 268 (2020)
589   122023.
590   [4] L. Dong, T. Xu, W. Chen, W. Lu, Synergistic multiple active species for the photocatalytic degradation
591   of contaminants by imidazole-modified $g-C_3N_4$ coordination with iron phthalocyanine in the presence of
592   peroxymonosulfate, Chemical Engineering Journal 357 (2019) 198-208.
593   [5] N. Ahmadpour, M.H. Sayadi, S. Sobhani, M. Hajiani, Photocatalytic degradation of model
594   pharmaceutical pollutant by novel magnetic TiO2@ ZnFe2O4/Pd nanocomposite with enhanced
595   photocatalytic activity and stability under solar light irradiation, Journal of Environmental Management
596   271 (2020) 110964.
597   [6] B. Poornaprakash, U. Chalapathi, M.C. Sekhar, V. Rajendar, S.P. Vattikuti, M.S.P. Reddy, Y. Suh, S.-H.
598   Park, Effect of Eu^{3+} on the morphology, structural, optical, magnetic, and photocatalytic properties of
599   ZnO nanoparticles, Superlattices and Microstructures 123 (2018) 154-163.
600   [7] A. Di Paola, E. García-López, G. Marcì, L. Palmisano, A survey of photocatalytic materials for
601   environmental remediation, Journal of hazardous materials 211 (2012) 3-29.
602   [8] B. Poornaprakash, U. Chalapathi, B.P. Reddy, S.P. Vattikuti, M.S.P. Reddy, S.-H. Park, Elemental,
603   morphological, structural, optical, and magnetic properties of erbium doped ZnO nanoparticles,
604   Materials Research Express 5(3) (2018) 035018.
605   [9] B. Poornaprakash, U. Chalapathi, K. Subramanyam, S.P. Vattikuti, S.-H. Park, Wurtzite phase Co-
606   doped ZnO nanorods: Morphological, structural, optical, magnetic, and enhanced photocatalytic
607   characteristics, Ceramics International 46(3) (2020) 2931-2939.
608   [10] D. Štrbac, C.A. Aggelopoulos, G. Štrbac, M. Dimitropoulos, M. Novaković, T. Ivetić, S.N.
609   Yannopoulos, Photocatalytic degradation of Naproxen and methylene blue: comparison between ZnO,
610   TiO_2 and their mixture, Process Safety and Environmental Protection 113 (2018) 174-183.
611   [11] H.B. Hadjltaief, M.B. Zina, M.E. Galvez, P. Da Costa, Photocatalytic degradation of methyl green dye
612   in aqueous solution over natural clay-supported $ZnO–TiO_2$ catalysts, Journal of Photochemistry and
613   Photobiology A: Chemistry 315 (2016) 25-33.
614   [12] A.A.M. Sakib, S.M. Masum, J. Hoinkis, R. Islam, M. Molla, A. Islam, Synthesis of CuO/ZnO
615   nanocomposites and their application in photodegradation of toxic textile dye, Journal of Composites
616   Science 3(3) (2019) 91.
617   [13] R. Ebrahimi, A. Maleki, Y. Zandsalimi, R. Ghanbari, B. Shahmoradi, R. Rezaee, M. Safari, S.W. Joo, H.
618   Daraei, S.H. Puttaiah, Photocatalytic degradation of organic dyes using WO_3-doped ZnO nanoparticles

fixed on a glass surface in aqueous solution, Journal of Industrial and Engineering Chemistry 73 (2019) 297-305.

[14] K.A. Adegoke, M. Iqbal, H. Louis, O.S. Bello, Synthesis, characterization and application of CdS/ZnO nanorod heterostructure for the photodegradation of Rhodamine B dye, Materials Science for Energy Technologies 2(2) (2019) 329-336.

[15] S. Vattikuti, Y.-J. Baik, C. Byon, Enhanced photocatalytic activity of MoO_3-supported SnO_2 composite synthesized by a wet chemical method, Materials Express 6(2) (2016) 161-174.

[16] K. Devarayapalli, S.P. Vattikuti, K.S. Yoo, P. Nagajyothi, J. Shim, Rapid microwave-assisted construction of ZIF-8 derived ZnO and ZnO@ Ta_2O_5 nanocomposite as an efficient electrode for methanol and urea electro-oxidation, Journal of Electroanalytical Chemistry 878 (2020) 114634.

[17] S.P. Vattikuti, P.A.K. Reddy, J. Shim, C. Byon, Visible-light-driven photocatalytic activity of SnO_2–ZnO quantum dots anchored on $g-C_3N_4$ nanosheets for photocatalytic pollutant degradation and H_2 production, ACS omega 3(7) (2018) 7587-7602.

[18] J. Vidic, S. Stankic, F. Haque, D. Ciric, R. Le Goffic, A. Vidy, J. Jupille, B. Delmas, Selective antibacterial effects of mixed ZnMgO nanoparticles, Journal of Nanoparticle Research 15(5) (2013) 1-10.

[19] M. Hassanpour, H. Safardoust-Hojaghan, M. Salavati-Niasari, Degradation of methylene blue and Rhodamine B as water pollutants via green synthesized Co_3O_4/ZnO nanocomposite, Journal of Molecular Liquids 229 (2017) 293-299.

[20] P. Lu, W. Zhou, Y. Li, J. Wang, P. Wu, Abnormal room temperature ferromagnetism in CuO/ZnO nanocomposites via hydrothermal method, Applied Surface Science 399 (2017) 396-402.

[21] M. Hassanpour, M. Salavati-Niasari, S.A. Mousavi, H. Safardoust-Hojaghan, M. Hamadanian, CeO_2/ZnO ceramic nanocomposites, synthesized via microwave method and used for decolorization of dye, Journal of Nanostructures 8(1) (2018) 97-106.

[22] A. Hamrouni, N. Moussa, F. Parrino, A. Di Paola, A. Houas, L. Palmisano, Sol–gel synthesis and photocatalytic activity of ZnO–SnO_2 nanocomposites, Journal of Molecular Catalysis A: Chemical 390 (2014) 133-141.

[23] R. Malik, P.S. Rana, V. Chaudhary, V.K. Tomer, S. Nehra, S. Duhan, Nanostructured WO_3/SnO_2 and TiO_2/SnO_2 Heterojunction with Enhanced Photocatalytic Performance, Energy and Environment Focus 5(2) (2016) 108-115.

[24] R. Saravanan, V. Gupta, V. Narayanan, A. Stephen, Visible light degradation of textile effluent using novel catalyst ZnO/γ-Mn_2O_3, Journal of the Taiwan Institute of Chemical Engineers 45(4) (2014) 1910-1917.

[25] R. Saravanan, S. Karthikeyan, V. Gupta, G. Sekaran, V. Narayanan, A. Stephen, Enhanced photocatalytic activity of ZnO/CuO nanocomposite for the degradation of textile dye on visible light illumination, Materials Science and Engineering: C 33(1) (2013) 91-98.

[26] S. Zinatloo-Ajabshir, M.S. Morassaei, O. Amiri, M. Salavati-Niasari, L.K. Foong, $Nd_2Sn_2O_7$ nanostructures: green synthesis and characterization using date palm extract, a potential electrochemical hydrogen storage material, Ceramics International 46(11) (2020) 17186-17196.

[27] B. Siripireddy, B.K. Mandal, Facile green synthesis of zinc oxide nanoparticles by *Eucalyptus globulus* and their photocatalytic and antioxidant activity, Advanced Powder Technology 28(3) (2017) 785-797.

[28] R. Rathnasamy, P. Thangasamy, R. Thangamuthu, S. Sampath, V. Alagan, Green synthesis of ZnO nanoparticles using *Carica papaya* leaf extracts for photocatalytic and photovoltaic applications, Journal of Materials Science: Materials in Electronics 28(14) (2017) 10374-10381.

[29] T. Karnan, S.A.S. Selvakumar, Biosynthesis of ZnO nanoparticles using rambutan (**Nephelium lappaceumL.**) peel extract and their photocatalytic activity on methyl orange dye, Journal of molecular Structure 1125 (2016) 358-365.

665 [30] C. Soto-Robles, O. Nava, A. Vilchis-Nestor, A. Castro-Beltrán, C. Gómez-Gutiérrez, E. Lugo-Medina,
666 A. Olivas, P. Luque, Biosynthesized zinc oxide using *Lycopersicon esculentum* peel extract for methylene
667 blue degradation, Journal of Materials Science: Materials in Electronics 29(5) (2018) 3722-3729.
668 [31] Y. Zheng, L. Fu, F. Han, A. Wang, W. Cai, J. Yu, J. Yang, F. Peng, Green biosynthesis and
669 characterization of zinc oxide nanoparticles using *Corymbia citriodora* leaf extract and their
670 photocatalytic activity, Green Chemistry Letters and Reviews 8(2) (2015) 59-63.
671 [32] S. Erentürk, E. Malkoç, Removal of lead (II) by adsorption onto *Viscum album L.*: Effect of
672 temperature and equilibrium isotherm analyses, Applied surface science 253(10) (2007) 4727-4733.
673 [33] K. Kolon, A. Samecka-Cymerman, A. Klink, A.J. Kempers, *Viscum album* versus host (Sorbus
674 aucuparia) as bioindicators of urban areas with various levels of pollution, Journal of Environmental
675 Science and Health, Part A 48(2) (2013) 205-210.
676 [34] M.A. Soobrattee, V.S. Neergheen, A. Luximon-Ramma, O.I. Aruoma, T. Bahorun, Phenolics as
677 potential antioxidant therapeutic agents: mechanism and actions, Mutation Research/Fundamental and
678 Molecular mechanisms of mutagenesis 579(1-2) (2005) 200-213.
679 [35] S. Aryal, M.K. Baniya, K. Danekhu, P. Kunwar, R. Gurung, N. Koirala, Total phenolic content,
680 flavonoid content and antioxidant potential of wild vegetables from Western Nepal, Plants 8(4) (2019)
681 96.
682 [36] J. Santhoshkumar, S.V. Kumar, S. Rajeshkumar, Synthesis of zinc oxide nanoparticles using plant leaf
683 extract against urinary tract infection pathogen, Resource-Efficient Technologies 3(4) (2017) 459-465.
684 [37] N. Verma, S. Yadav, B. Marí, A. Mittal, J. Jindal, Synthesis and charcterization of coupled ZnO/SnO_2
685 photocatalysts and their activity towards degradation of cibacron red dye, Transactions of the Indian
686 Ceramic Society 77(1) (2018) 1-7.
687 [38] N. Ahmadpour, M.H. Sayadi, V. Anoop, B. Mansouri, Ultrasonic degradation of ibuprofen from the
688 aqueous solution in the presence of titanium dioxide nanoparticles/hydrogen peroxide, Desalination and
689 Water Treatment 145 (2019) 291-299.
690 [39] W.-D. Oh, Z. Dong, G. Ronn, T.-T. Lim, Surface–active bismuth ferrite as superior peroxymonosulfate
691 activator for aqueous sulfamethoxazole removal: performance, mechanism and quantification of sulfate
692 radical, Journal of hazardous materials 325 (2017) 71-81.
693 [40] F. Shahidi, P. Ambigaipalan, Phenolics and polyphenolics in foods, beverages and spices: Antioxidant
694 activity and health effects–A review, Journal of functional foods 18 (2015) 820-897.
695 [41] A. Karagöz, E. Önay, N. Arda, A. Kuru, Antiviral potency of mistletoe (*Viscum album ssp. album*)
696 extracts against human parainfluenza virus type 2 in Vero cells, Phytotherapy Research 17(5) (2003) 560-
697 562.
698 [42] S. Žilić, Phenolic compounds of wheat. Their content, antioxidant capacity and bioaccessibility, MOJ
699 Food Processing & Technology 2(3) (2016) 00037.
700 [43] W. Pietrzak, R. Nowak, M. Olech, Effect of extraction method on phenolic content and antioxidant
701 activity of mistletoe extracts from *Viscum album* subsp. abietis, Chemical Papers 68(7) (2014) 976-982.
702 [44] V. Katalinic, M. Milos, T. Kulisic, M. Jukic, Screening of 70 medicinal plant extracts for antioxidant
703 capacity and total phenols, Food chemistry 94(4) (2006) 550-557.
704 [45] J. Piechocka, K. Szymandera-Buszka, J. Kobus-Cisowska, A. Gramza-Michałowska, A. Jędrusek-
705 Golińska, The effect of thiamine concentration on the antioxidative activity indices in *tea* extracts,
706 Antioxidants 8(11) (2019) 555.
707 [46] M. Gulluce, F. Sahin, M. Sokmen, H. Ozer, D. Daferera, A. Sokmen, M. Polissiou, A. Adiguzel, H.
708 Ozkan, Antimicrobial and antioxidant properties of the essential oils and methanol extract from *Mentha
709 longifolia L.* ssp. longifolia, Food chemistry 103(4) (2007) 1449-1456.
710 [47] R. Karamian, M. Asadbegy, Antioxidant activity, total phenolic and flavonoid contents of three
711 *Onobrychis* species from Iran, Pharmaceutical sciences 22(2) (2016) 112-119.

712 [48] K. Saeedi, R. Omidbaigi, Determination of phenolics, soluble carbohydrates, carotenoid contents
713 and minerals of dog rose (*Rosa canina L.*) fruits grown in south-west of Iran, Iranian Journal of Medicinal
714 and Aromatic Plants 25(2) (2009) 203-215.
715 [49] K. Asha, G. Sucheta, M. Kavita, D. Nirmala, S. Jyoti, Quantification of phenolics and flavonoids by
716 spectrophotometer from-Juglans regia, International Journal of Pharma and Bio Sciences 1(3) (2010).
717 [50] Q.D. Do, A.E. Angkawijaya, P.L. Tran-Nguyen, L.H. Huynh, F.E. Soetaredjo, S. Ismadji, Y.-H. Ju, Effect
718 of extraction solvent on total phenol content, total flavonoid content, and antioxidant activity of
719 *Limnophila aromatica*, Journal of food and drug analysis 22(3) (2014) 296-302.
720 [51] M.T. Uddin, Y. Nicolas, C. Olivier, T. Toupance, L. Servant, M.M. Muller, H.-J. Kleebe, J. Ziegler, W.
721 Jaegermann, Nanostructured SnO_2–ZnO heterojunction photocatalysts showing enhanced
722 photocatalytic activity for the degradation of organic dyes, Inorganic chemistry 51(14) (2012) 7764-
723 7773.
724 [52] D. Chen, L. Gao, Novel synthesis of well-dispersed crystalline SnO_2 nanoparticles by water-in-oil
725 microemulsion-assisted hydrothermal process, Journal of colloid and interface science 279(1) (2004)
726 137-142.
727 [53] D.J. Sornalatha, P. Murugakoothan, Room temperature synthesis of ZnO nanostructures using CTAB
728 assisted sol-gel method for application in solar cells, International journal of emerging technology and
729 advanced engineering 3(9) (2013) 414-418.
730 [54] P. Jamdagni, P. Khatri, J. Rana, Green synthesis of zinc oxide nanoparticles using flower extract of
731 *Nyctanthes arbor-tristis* and their antifungal activity, Journal of King Saud University-Science 30(2)
732 (2018) 168-175.
733 [55] C. Shifu, C. Lei, G. Shen, C. Gengyu, The preparation of coupled WO_3/TiO_2 photocatalyst by ball
734 milling, Powder technology 160(3) (2005) 198-202.
735 [56] A. Babar, S. Shinde, A. Moholkar, C. Bhosale, J. Kim, K. Rajpure, Structural and optoelectronic
736 properties of antimony incorporated tin oxide thin films, Journal of Alloys and Compounds 505(2) (2010)
737 416-422.
738 [57] G. Ballerini, K. Ogle, M.-G. Barthés-Labrousse, The acid–base properties of the surface of native zinc
739 oxide layers: an XPS study of adsorption of 1, 2-diaminoethane, Applied surface science 253(16) (2007)
740 6860-6867.
741 [58] G. Li, M.K. Leung, Template-free synthesis of hierarchical porous SnO_2, Journal of sol-gel science and
742 technology 53(3) (2010) 499-503.
743 [59] N. Ahmadpour, M.H. Sayadi, S. Homaeigohar, A hierarchical Ca/TiO_2/NH_2-MIL-125 nanocomposite
744 photocatalyst for solar visible light induced photodegradation of organic dye pollutants in water, RSC
745 Advances 10(50) (2020) 29808-29820.
746 [60] A. Garg, T. Singhania, A. Singh, S. Sharma, S. Rani, A. Neogy, S.R. Yadav, V.K. Sangal, N. Garg,
747 Photocatalytic degradation of bisphenol-A using N, Co Codoped TiO_2 catalyst under solar light, Scientific
748 reports 9(1) (2019) 1-13.
749 [61] E.J. Rosenfeldt, K.G. Linden, Degradation of endocrine disrupting chemicals bisphenol A, ethinyl
750 estradiol, and estradiol during UV photolysis and advanced oxidation processes, Environmental Science
751 & Technology 38(20) (2004) 5476-5483.
752 [62] F. Poorsajadi, M.H. Sayadi, M. Hajiani, M.R. Rezaei, Synthesis of CuO/Bi_2O_3 nanocomposite for
753 efficient and recycling photodegradation of methylene blue dye, International Journal of Environmental
754 Analytical Chemistry (2020) 1-14.
755 [63] M.H. Sayadi, N. Ahmadpour, S. Homaeigohar, Photocatalytic and Antibacterial Properties of Ag-
756 CuFe2O4@ WO3 Magnetic Nanocomposite, Nanomaterials 11(2) (2021) 298.
757 [64] M. Thomas, G.A. Naikoo, M.U.D. Sheikh, M. Bano, F. Khan, Effective photocatalytic degradation of
758 Congo red dye using alginate/carboxymethyl cellulose/TiO_2 nanocomposite hydrogel under direct
759 sunlight irradiation, Journal of Photochemistry and Photobiology A: Chemistry 327 (2016) 33-43.

760   [65] M. Dehghani, S. Nasseri, M. Ahmadi, M.R. Samaei, A. Anushiravani, Removal of penicillin G from
761   aqueous phase by Fe^{+3}-TiO_2/UV-A process, Journal of Environmental Health Science and Engineering
762   12(1) (2014) 1-7.
763   [66] S.H. Borji, S. Nasseri, A.H. Mahvi, R. Nabizadeh, A.H. Javadi, Investigation of photocatalytic
764   degradation of phenol by Fe (III)-doped TiO_2 and TiO_2 nanoparticles, Journal of Environmental Health
765   Science and Engineering 12(1) (2014) 1-10.
766   [67] J. Grzechulska, A.W. Morawski, Photocatalytic labyrinth flow reactor with immobilized P25 TiO_2 bed
767   for removal of phenol from water, Applied Catalysis B: Environmental 46(2) (2003) 415-419.
768   [68] M.H. Sayadi, S. Sobhani, H. Shekari, Photocatalytic degradation of azithromycin using GO@
769   Fe3O4/ZnO/SnO2 nanocomposites, Journal of Cleaner Production 232 (2019) 127-136.
770   [69] A. Takdastan, B. Kakavandi, M. Azizi, M. Golshan, Efficient activation of peroxymonosulfate by using
771   ferroferric oxide supported on carbon/UV/US system: a new approach into catalytic degradation of
772   bisphenol A, Chemical Engineering Journal 331 (2018) 729-743.
773   [70] F. Liu, T. He, Q. Cao, Y. Xu, W. Liu, W. Zhou, Structure and Property of Nano-TiO_2 Doped with Ag^+
774   Membrane Photocatalyst, Journal of nanoscience and nanotechnology 15(4) (2015) 2726-2732.
775   [71] W. Ali, H. Ullah, A. Zada, M.K. Alamgir, W. Muhammad, M.J. Ahmad, A. Nadhman, Effect of
776   calcination temperature on the photoactivities of ZnO/SnO_2 nanocomposites for the degradation of
777   methyl orange, Materials Chemistry and Physics 213 (2018) 259-266.

778